Implementation and study of quasi two dimensional thin film field effect transistors

Sven Renkert

IMPLEMENTATION AND STUDY OF QUASI TWO DIMENSIONAL THIN FILM FIELD EFFECT TRANSISTORS

SVEN RENKERT

Doctoral thesis in the framework of a french-german cooperation

January 2021

French Supervisor
Dr. Jean-Luc Bubendorff
Centre national de la recherche scientifique
Institut de Science des Matérieux de Mulhouse
Université de Haute-Alsace

German Supervisor
Prof. Günter Reiter
Fakultät für Mathematik und Physik
Physikalisches Institut
Albert-Ludwigs-Universität Freiburg

We don't have enough lives to base *all* our decisions on the statistically expected outcome.

— Unknown

In loving memory of my grandma

ABSTRACT

Fabricating organic Field Effect Transistor (FET)s can be achieved easily and cost effectively by depositing thin films of the organic semiconductor on top of a silicon wafer with a suitably thick oxide layer (about 100 nm to 200 nm). In order to achieve high charge carrier mobilities in organic semiconductor materials, the molecular order in the device plays a crucial role, with higher order typically leading to higher mobilities and thus better performance of the device. However, most organic semiconductor materials dewet on silicon wafers with such thick oxide layers, and dewetting can limit the possibility of crystallizing thin film organic semiconductors. This undesired phenomena importantly affects the mobility in these systems, as the formation of individual droplets due to dewetting often introduces grain boundaries between crystals, thus severely limiting large scale order and charge carrier transport. In this study, we used an oligothiophene called 5TBT. It is based on 5 monomer units each consisting of two thiophene rings surrounding a benzene ring. We present a method to crystallize structures with a unique orientation up to the mm scale, despite the fact that films of this molecule dewet into pancake structures on silicon wafers with thick oxide layers when molten. One important advantage of this method is that it can be easily extended to other molecules besides the oligothiophene studied here, as the prerequisites are based on strong anisotropy in the growth speed of the crystalline faces. We expect other organic molecules with anisotropic crystal growth (e. g. molecules exhibiting π-stacking) to be suitable candidates for this method. We present the first realization of FETs with 5TBT based on this method. The extracted hole mobilities are two orders of magnitude higher compared to non-crystallized films.

Additionally, we observed a very thin film of molecules connecting the pancake structures after dewetting. This film seems to be ordered, as the hole mobility measured in a FET configuration exceeds the mobility obtained from an amorphous film by and order of magnitude. The formation of this film can be suppressed by illuminating the sample with a light source (e. g. a microscope), and seems to play a crucial role in crystal growth, as crystal growth stops without such a layer.

Compared to their inorganic counterparts, most organic FETs react sensitively to the presence of adsorbates, depending strongly on their physical and chemical interactions. This effect is commonly used in sensor systems to detect the presence of target molecules in gases or liquids, called chemical noses and tongues, respectively. As the FETs designed in this study are stable in air for more then a month, we tested them as chemical noses for acetone and 2,4-Dinitrotoluene (DNT). The FETs show a strong sensitivity with respect to acetone, surpassing the sensitivity of Poly(3-hexylthiophene-2,5-diyl) (P_3HT). 5TBT is insensitive towards DNT, which is surprising, as 5TBTs fluorescence is strongly quenched by DNT in solution.

ZUSAMMENFASSUNG

Organische Feldeffekt-Transistoren (FETs) können einfach und kostengünstig hergestellt werden, indem man dünne Filme eines organischen Halbleitermaterials auf die Oberfläche eines Siliziumswafers mit geeigneter Oxidschichtdicke (etwa 100 nm bis 200 nm) aufbringt.

Bei der Aufgabe, hohe Ladungsträgermobilitäten in organischen Halbleitermaterialien zu erreichen, spielt die Ordnung der Moleküle eine entscheidende Rolle, wobei eine Erhöhung der Ordnung typischerweise zu höheren Mobilitäten und damit besserer Effizienz eines Endgerätes führt.

Allerdings entnetzen die meisten organische Halbleitermaterialien auf Siliziumwafern mit solch dicken Oxidschichten, und die Entnetzung kann die Möglichkeiten der Kristallisation eines Dünnschichthalbleiters drastisch einschränken. Dieses unerwünschte Phänomen beeinflusst die Mobilität in solchen Systemen, da die einzelnen Tröpfchen, die durch die Entnetzung entstanden sind, neue Korngrenzen zwischen Kristallen darstellen, und dadurch die Ordnung und den Ladungsträgertransport auf großen Skalen stark einschränken.

In dieser Arbeit wird ein Oligotheophen names 5TBT untersucht. Es basiert auf 5 Monomeren welche wiederum aus einem von zwei Theophenringen umschlossenen Benzolring bestehen. Hier wird eine Methode vorgestellt, mit welcher kristalline Strukturen mit einer einzigen Vorzugsrichtung mit einer Größe im Bereich von mm hergestellt werden können, obwohl die Filme aus diesem Molekül zu Pfannkuchenstrukturen entnetzen, wenn sie auf Siliziumwafern mit dicken Oxidschichten geschmolzen werden.

Ein wichtiger Vorteil dieser Methode besteht darin, dass sie einfach auf andere Moleküle neben dem hier untersuchten Oligotheophen ausgeweitet werden kann, da die Vorraussetzungen nur auf der starken Anisotropie der Wachstumsgeschwindigkeiten entlang verschiedener Kristallorientierungen beruhen. Es ist zu erwarten, dass andere organische Moleküle mit anisotropem Kristallwachstum (wie beispielsweie Moleküle die mittels π-π-Wechselwirkung wachsen) geeignete Kandidaten für diese Methode sind.

Es wird die erste Herstellung eines auf dieser Methode basierenden FETs aus 5TBT präsentiert. Die extrahierten Mobilitäten für Elektronen-

Löcher liegen zwei Größenordnungen über jenen nichtkristalliner Filme.

Zudem wurde nach der Entnetzung ein dünner molekularer Film zwischen den Pfannkuchenstrukturen beobachtet. Auch in diesem Film scheinen die Moleküle geordnet zu sein, da die Mobilitäten der Löcher in einem FET-Aufbau die Mobilität eines amorphen Filmes um eine Größenordnung übersteigt. Die Bildung eines solchen Filmes kann durch Bestrahlung mit Licht aus einer Lichtquelle (zum Beispiel eines Lichtmikroskopes) unterdrückt werden, und scheint eine entscheidende Rolle beim Kristallwachstum zu spielen, da ohne eine solche Schicht das Kristallwachstum unterbunden wird.

Im Gegensatz zu anorganischen Halbleitern reagieren die meisten FETs auf Basis organischer Halbleiter auf die Anwesenheit von adsorbierten Molekülen, wobei dies stark von deren physikalischen und chemischen Wechselwirkungen abhängt. Dieser Effekt wird üblicherweise in Sensorsystemen verwendet, um die Konzentration eines Schlüsselmoleküls in Gasen oder Flüssigkeiten zu messen. Diese werden entsprechend Chemische Nasen beziehungsweise Chemische Zungen genannt. Da die hier hergestellten FETs bei Raumbedingungen über mehrere Monate stabil bleiben, wurden sie auf die Detektion von Aceton und Dinitrotoluol (DNT) getestet. Die FETs zeigen eine stärkere Sensitivität gegenüber Aceton als P3HT. Überraschenderweise ist 5TBT insensitiv gegenüber DNT, obwohl dessen Fluoreszenz stark zurückgeht, wenn 5TBT in Lösung mit DNT in Kontakt kommt.

RÉSUMÉ

L'un des enjeux essentiels dans le domaine de l'électronique moléculaire est de réussir à réaliser des films minces organiques semiconducteurs parfaitement cristallisés sur des oxydes thermiques sur wafers de silicium. Ces films doivent présenter des fortes mobilités électriques afin d'obtenir un transistor à effet de champ (FET) performant. Or, la plupart des matériaux organiques utilisés dans la littérature, ne mouille pas ce type de substrat limitant ainsi fortement la mobilité électrique. Ce travail de thèse a permis de lever cette difficulté grâce à une méthode de cristallisation qui permet de réaliser des couches organiques présentant une seule orientation cristallographique sur des domaines d'une surface de l'ordre du mm2. Le processus expérimental proposé se généralise facilement à des systèmes moléculaires autres que les oligothiophenes employés dans ce mémoire puisqu'il suppose uniquement une forte anisotropie des vitesses de croissance cristallines dans deux différentes directions de croissance. C'est le cas par exemple pour tous les systèmes dont la croissance fait appel à des interactions π-π entre molécules voisines. Nous avons également réalisé et caractérisé des transistors à effet de champ obtenus par cette méthode. Ils présentent des mobilités de deux ordres de grandeurs au-dessus de celle des films non cristallisés. Nous avons mis en évidence l'existence d'une monocouche supramoléculaire d'interface présentant une forte conductivité. Celle-ci interconnecte, non seulement électriquement mais aussi en terme d'orientation cristalline, des domaines de croissance qui ont l'air spatialement séparés lorsque nous les observons en microscopie optique et en microscopie à force atomique. Cette couche conduit à une mobilité de trous en configuration FET d'un ordre de grandeur supérieur à celle d'un film amorphe. L'un des avantages pratiques d'une structure FET utilisant un film mince organique est que ce type de dispositif est très sensible à la présence d'adsorbats, et de ce fait peut servir de détecteur de molécules cibles dans un environnement liquide ou gazeux. Puisque nos dispositifs FET sont stables à l'air, nous avons testé leur efficacité de détection de molécules cibles comme l'acétone et le 2,4-Dinitrotoluene (DNT). Notre détecteur est insensible au DNT porté par un gaz inerte alors que la fluorescence des oligothiophènes employés est fortement atténuée en milieu liquide par le DNT. Par contre, nous mettons en

évidence une très forte sensibilité à l'acétone de notre détecteur de gaz bien plus importante que celle des détecteurs utilisant le Poly(3-hexylthiophene-2,5-diyl) ou P3HT, un standard en détecteur à base de polymères conducteurs.

PUBLICATIONS

Some ideas and figures have appeared previously in the following publication:

A new growth process for crystalline ultra-thin layers of conjugated oligomers used in Field-Effect Transistor applications (in review)

CONTENTS

LIST OF FIGURES

ACRONYMS

SPM Scanning Probe Microscopy

AFM Atomic Force Microscopy

AM AFM Amplitude Modulation AFM

FM AFM Frequency Modulation AFM

CAFM Conductive Atomic Force Microscopy

KPFM Kelvin Probe Force Microscopy

STM Scanning Tunneling Microscopy

PSD Position Sensitive Device

FET Field Effect Transistor

OFET Organic Field Effect Transistor

UHV Ultra High Vacuum

DNT 2,4-Dinitrotoluene

MFC Mass Flow Controller

DC Detector Chamber

AC Analyte Chamber

SCLC Space Charge Limited Current

P3HT Poly(3-hexylthiophene-2,5-diyl)

SVA Solvent Vapour Annealing

1

MOTIVATION

Organic electronics, such as perovskites and organic semiconducting polymers, were thought to be impossible until about 1960. Today, it has found many applications (e. g. organic solar cells in textiles, flexible screens) and become an active field of research for various reasons beyond curiosity: Compared to silicon based semiconductors, manufacturing costs are considerably lower, and the resulting devices are much more flexible, both mechanically and concerning electro-optical properties such as e. g. tunable band gaps. In addition, some effects like e. g. chemical sensing of target molecules in a lock-and-key principle are unique to the chemical structure of the organic semiconductor. As even small changes in the chemical structure of a molecule can drastically change the macroscopic material properties, the unlimited number of combinations in chemistry allows for a similar variety in material properties, most of which still wait to be discovered.

Field effect transistors, light emitting diodes and solar cells based on organic semiconductors are available commercially, and many applications have been found thanks to the unique properties of these materials, such as e. g. fabric coated with organic solar cells in order to charge a smartphone, or surface coatings for windows in smart homes, allowing to drastically change the transparency and/or color by applying a small voltage. However, inorganic semiconductors still perform considerably better concerning charge carrier mobilities and efficiency. Comparing the current efficiency of organic solar cells to the efficiency of photosynthesis, we can safely assume that a huge potential remains. Despite considerable efforts and progress in the field, the method of trial and error prevails in research about the structure property relationship, as the link between chemical structure and macroscopic properties is still obscure. In fact, the complexity of the problem arises from the seemingly endless possible combinations of chemical building blocks, and the notion of a single link may be misleading. At the current state of the art, precisely controlling the structure in the nano- and micro scale seems to be easier than predicting the resulting macroscopic properties. Thus, the fabrication of a high performing device or one with a very specific purpose remains

difficult, as even minor changes in the chemical structure may or may not lead to drastic changes of the macroscopic properties.

This study focuses on the structure function relationship of a new organic semiconductor named 5TBT. Based on its chemical structure, it promises interesting charge carrier properties and chemical sensing behavior. The general goal of this thesis is the characterization of these properties by applying the first field effect transistor based on a large scale crystalline film build from 5TBT. Then, the mobility and its chemical sensing capabilities are probed.

With a few noticeable exceptions, crystallization of both small molecules and polymers usually leads to enhanced charge carrier mobility, often by orders of magnitude. When fabricating a device, e. g. a Field Effect Transistor (FET), crystallization is easily achieved by heating the film above its melting temperature and subsequent quenching and holding it at the desired (lower) crystallization temperature until the material is crystallized. For some molecules, more advanced techniques can achieve oriented growth of the crystals. A common approach to building FETs is to spin coat or drop cast a film onto a (doped) silicon wafer with a thick oxide layer, as the substrate can be directly used as the gate contact in a bottom gate top contact device. However, when using silicon wafers with an oxide layer, organic molecules tend to dewet as soon as one heats them above melting temperature. Dewetting occurs when the van der Waals forces between the molecules are stronger than the van der Waals forces between molecule and substrate. Then, previously homogeneous films rupture and form patterns of droplets or pancakes. This is especially pronounced for relatively short molecules like 5TBT. The formation of such patterns can significantly hinder crystal growth into large scale structures. However, in this thesis we discuss a method of growth of large scale structures even after dewetting, which was not described before.

2

INTRODUCTION

The background of techniques, methods and the molecule used is summarized in this chapter. At first, we will present the theory of dewetting. Then, the molecule family is presented, including a summary of previously conducted studies on the subject. A brief summary of the developments from Scanning Tunneling Microscopy (STM) over Atomic Force Microscopy (AFM) to the principles of qPlus, a technique combining both STM and AFM, follows. Then, we describe the use of crossed polarizers in optical microscopy. The chapter ends with a description of the working principle of organic field effect transistors.

2.1 DEWETTING

When bringing a liquid into contact with a surface, we can observe two distinct behaviors: if the adhesive forces are stronger than the cohesive forces, the liquid spreads over the surface, in case it is vice versa, the liquid forms droplets in the shape of a spherical cap on the surface. For simplicity, we consider only liquids on solid surfaces here, but similar principles govern liquid liquid interfaces.

When cohesive forces are stronger than adhesive forces, a characteristic contact angle θ at the edge of a spherical cap is determined by the surface tensions γ between liquid and solid, liquid and gas, and solid and gas. The spreading coefficient S is defined as

$$S = \gamma_{SG} - \gamma_{SL} - \gamma_{LG} \tag{1}$$

The spreading coefficient is a useful measure to characterize the behavior of a liquid on a film. If it is positive, the liquid spreads over the surface and covers it, we say the liquid wets the surface. If S is negative, the liquid forms spherical caps, e. g. mercury on glass and water on Teflon dewet. The well known and intensively studied lotus effect[3] is based on the same principle, using very large negative spreading coefficients.

The contact angle θ between the spherical cap and the surface can be determined by a consideration of forces acting on the edge of the

droplet in equilibrium. The forces caused by the surface tension at the interfaces are balanced, and thus sum to zero:

$$\gamma_{SG} + \gamma_{SL} + \cos(\theta)\gamma_{LG} = 0 \tag{2}$$

Depending on the contact angle, the liquid may adopt different shapes. For contact angles $\theta > 90\,\text{deg}$, the shape is called droplet. For very small contact angles, as we observe in this study, the spherical caps resemble pancakes.

In many cases, non-equilibrium states can be observed, where the liquid is not in the form of a droplet, even though it is the energetically favorable state. Considering coatings and thin films in general, the material is often present in the state of a solid homogeneous film, before being molten. Then, the liquid film will still remain homogeneous initially, but given enough time it will reach towards its equilibrium configuration. This process is called dewetting.

When preparing a thin polymer film for the application of a Field Effect Transistor (FET), those films are usually solid at room temperature. In order to crystallize such a film (enhancing its order and thus mobility), one has to melt the film at higher temperatures. If the spreading coefficient is negative, as is true for most organic semiconductors on SiO, the configuration of spherical caps is energetically preferred over a film. However, even for negative surface coefficients a system may stay in the shape of a film. If the film thickness h is sufficiently large, a film will not dewett. Considering films below a critical height h_c, given enough time the liquid eventually will form spherical caps with the characteristic contact angle for the system. Two scenarios of dewetting can be distinguished: dewetting via nucleation of a hole and subsequent growth, and spinodal dewetting. In the first scenario, the process governing nucleation can be further distinguished between thermal and heterogeneous nucleation. Figure 1 compares AFM snapshots of all three cases.

Heterogeneous nucleation (c) occurs from defects in the surface, e. g. dust particles. As this process is based on the initiation of nuclei at a random place but at a specific time, and all holes grow with the same speed, holes will be randomly distributed but having the same size. When thermal nucleation (b) dominates the formation of nuclei through thermal motion, not only the place but also the time of formation of a hole is random. Thus, when taking a snapshot holes have random positions and differ in size. In both cases (b) and (c), holes grow by retracting the edge and therefore forming an elevated

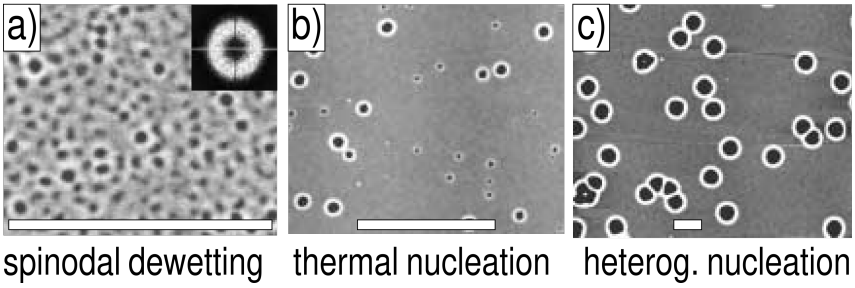

Figure 1 – Comparison of different dewetting processes: spinodal dewetting, thermal and heterogeneous nucleation, taken from [43]

rim with higher thickness. This can be seen as a white line in Figure 1 (b) and (c). At one point in time, the liquid has retracted from most parts of the surface and the rims will meet (coalesce) with their next neighbors, forming a polygonal structure of liquid rims. These rims subsequently decay into individual droplets and thus finally reach the equilibrium state as discussed above. Due to the characteristic formation process, droplets will be aligned in the polygonal shape of the connected rims.

In the second scenario, spinodal dewetting, small perturbations of the surface of the liquid get enhanced by the difference in capillary forces on the curved surface[51]. Initial small perturbations of the surface grow with a specific wavelength, thus the resulting spherical caps have similar size and are evenly distributed in space. The inset in Figure 1 (a) shows a 2D-Fourier transformation of the AFM image. The ring seen in the Fourier transformation visualizes the predominant wavelength clearly. This wavelength depends on the initial thickness of the film, increasing with increasing film thickness. A transition from dewetting via spinodal dewetting towards nucleation and growth is expected with increasing film thickness. Also, as an increase of polymer length (molecular weight) results in higher viscosity, films containing longer polymer chains are dominated by nucleation and growth rather than spinodal dewetting[51]. In addition, polymers may exhibit additional effects due to their chain-like structure[13, 41]. In this study, we use both a rather short oligomer with just 5 repeat units and aim at the formation of crystals with just a few layers of molecules, thus expecting spinodal dewetting.

2.2 CHARACTERISTICS OF TBT

The molecule studied belongs to a family of molecules called TBT. This is a shorthand for the monomer structure, consisting of 2 thiophene rings on opposite sides of a benzene ring. It was shown that the molecule can be synthesized with various side chains and with a variety of defined lengths. Oligomers with a length ranging from 1 to 40 repeat units and with different side chains attached to the benzene rings were used in previous studies. In this study, we focus on the molecule with an ethyl-hexyl side chain and 5 monomers. This document always refers to the subfamily of TBT molecules with ethyl-hexyl side chains, except when otherwise mentioned explicitly. The full chemical structure of 5TBT is depicted in Figure 2, the leftmost monomer is surrounded by a blue box. Each monomer contains a benzene ring with a thiophene on opposing sides, forming the backbone of the polymer structure, and two side chains linked to the benzene via oxygen atoms.

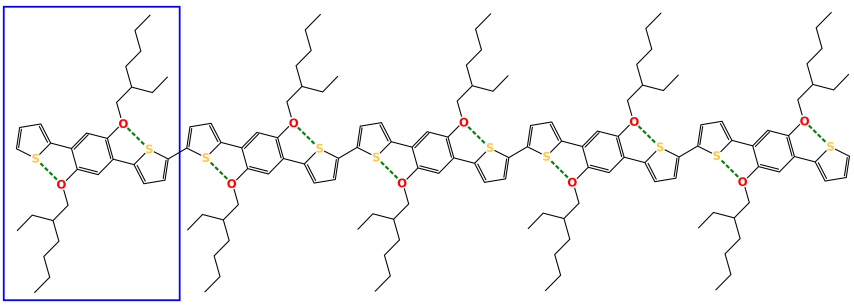

Figure 2 – Chemical structure of the 5TBT molecule.

Previous studies have shown that sulfur-oxygen bonds form between the sulfur in the thiophene and the oxygen in the benzene-1,4-diol rings [30, 35, 40], as represented by green dotted lines in Figure 2. These bonds stabilize the backbone against rotation and make the backbone relatively stiff, which in turn leads to a strong conjugation along the backbone. Fully stretched, a single molecule of 5TBT is about 6 nm long and the side chains span over a distance of about 2 nm.

Interesting optoelectric properties of the molecules were found [33, 45]. In one study 3TBT molecules with an octyl side chain were evaporated onto graphene in a Ultra High Vacuum (UHV)-chamber. The molecules self assemble such that the backbones lie in continuation of each other. In this configuration, the end thiophene rings can

connect, forming supramolecular conjugated pathways over several molecules[45].

Single crystal needles grown from 3TBT with octyl side chains have been proven to act as a wave guide[33] due to their highly ordered backbones.

5TBT has a molar mass of 2480 g mol^{-1}. The melting point of 186 °C was measured by observation of the melting process of a thin film on a hot stage under a microscope. As received from synthesis, it forms dark red, brittle aggregates. The flat, plate-like aggregates form a powder with grain size of 0.1 mm to 1 mm. 5TBT is soluble in many organic solvents, most notably for this study in toluene and dodecane, and thus it can be easily processed by e. g. spin coating, drop casting and printing techniques.

Thermogravimetric analysis of 5TBT has shown good stability up to 325 °C. The weight loss of 67% can be attributed to the decomposition of the ((2-ethyl)-hexyloxy) solubilizing side chains. This result is in great accordance with what was reported for poly(1,4-bis-[2-(4-hexylthiophene)]-2,5-dimethylphenylene[39].

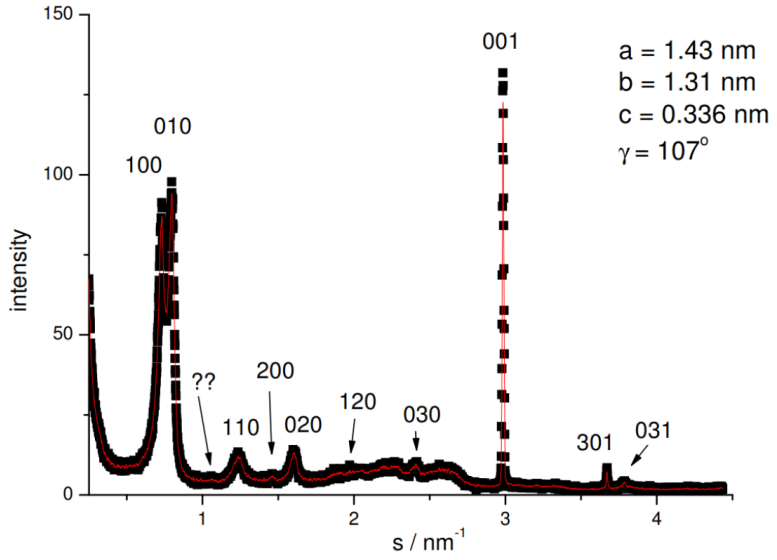

Figure 3 – Diffraction analysis of 5TBT.

Figure 3 shows the diffraction analysis of 5TBT in a several µm thick film. The sample was prepared by repeatedly dropcasting highly concentrated solution of 5TBT in toluene with an intermediate drying step onto a silicon waver. During drying, the molecules formed randomly oriented small crystallites within the thick film. Wide-angle X-ray scattering (WAXS) measurements were performed with a mod-

ified Siemens D500 X-ray diffractometer with a conventional Cu K α X-ray source of wavelength $\lambda = 0.1542\,nm$. The unit cell parameters a, b, c and γ can explain the observed peak structure with the given peak orientations. The unit cell parameter $a = 1.4\,nm$ can be related to the distance between stacked side chains. This value suggests a slight interdigitation between side chains. The unit cell parameter $b = 1.3\,nm$ compares favorably with the size of a single TBT monomer unit. The unit cell parameter $c = 0.34\,nm$ strongly suggests π-π-stacking between 5TBT molecules.

2.3 USE OF CROSSED POLARIZERS IN MICROSCOPY

In optical microscopy, many different techniques can be used to enhance contrast between the objects under study and the background. In bright field microscopy, contrast arises from differences in absorbance of the material, thus it is best suited if the objects under study differ in absorbance from the background. In dark field microscopy, where the light coming directly from the sample is blocked from view, the contrast comes from scattered light. Thus, dark field microscopy is best suited for the investigation of light scattering objects. A Fluorescence microscope illuminates the sample with a specific wavelength, while filtering this wavelength from the view. Thus, only fluorescent objects appear in the image with strong contrast.

In order to enhance contrast based on birefringence, two polarizers are mounted perpendicular (crossed) to each other into the light path of the microscope. The first polarizer serves to illuminate the sample with linear polarized light of a specific orientation. The second polarizer filters this specific orientation from the magnified view, resulting in a black image when the direction of polarization is not altered by the objects in the field of view. This second polarizer is called analyzer, as it bases the contrast of objects on their birefringence properties.

When polarized light passes through a birefringent object, its polarization direction is changed based on the thickness of the object, the wavelength of the light and the birefringence. When the polarization of the light matches the optical axis or is perpendicular to the optical axis, the polarization direction is not changed and no light is transmitted to the view. When rotating a birefringent object under crossed polarizers, these four perpendicular positions where the object appears black are called extinction positions. In the diagonal

position with a 45° angle to the extinction position the highest intensity is observed. This pattern is used to identify birefringent objects and the orientation of their optical axis. For organic semiconductors, this can be used as a tool to investigate the degree of order in the crystal[32].

2.4 SCANNING PROBE MICROSCOPY

Scanning Probe Microscopy (SPM) is a term used for a large set of surface imaging methods. In all of them, the basic idea is to scan over a surface with a tip while measuring a specific interaction between tip and surface. The interactions used in SPM range from tunneling current over interatomic forces to electrostatic potential and magnetic interactions. Most SPM-techniques are named after the respective interaction used in the set-up: The two most commonly used interactions are the tunneling current between tip and surface and the force between them, respectively. The first technique is called STM, the latter AFM.

Measuring the interaction strength at each point of a line wise scan allows to present these measured data points in two-dimensional images, where the range of measured interaction strength can be mapped by a false color code, analogous to the use of hypsometric tints in maps. As the data acquired during such a scan usually contains more information than the mere distance between tip and sample, SPM images often show aspects of the surface that go far beyond its mere topography.

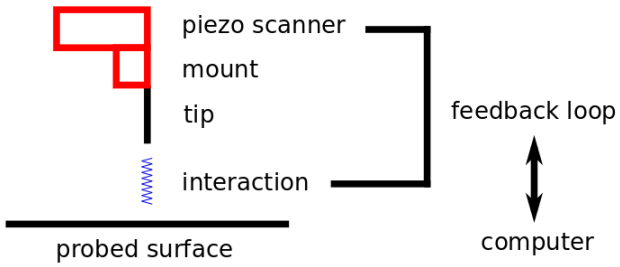

Figure 4 – A sketch of the working principle of SPM

Figure 4 shows a schematic drawing of the general setup of SPM. The piezo scanner is capable of positioning the tip precisely by using the piezo effect. Typically, it consists out of three piezo elements attached to each other orthogonally, thus controlled elongation in all three spatial directions is possible by applying appropriate voltages

at the corresponding piezo element. Nowadays, piezo scanners from a single piezo element with contacts applied in different spatial directions are commercially available, too. Elongation of the piezo scanner along the direction of the tip controls the distance between tip and surface. Elongation orthogonal to this allows to position the tip at a specific point over the surface, and is used to execute the scanning motion. Piezo scanners typically exhibit responses in the order of a few $\mathrm{nm\,V^{-1}}$[9], allowing to position the tip with sub nm precision.

The type of mount can differ considerably between different SPM techniques. For STM, the tip is simply glued to the scanner; for AFM, it is usually mounted to a cantilever, which itself plays a crucial role in the measurement process of the interaction strength. The mounting can be a complex part of the technique, as we will discuss in more detail later, e. g. on the example of qPlus.

Generally the strength of the interaction between tip and surface changes when moving the scanner. These changes may arise due to changes in topography or material properties. In the most basic setup called constant-height mode, the scanner is moved over the surface, while the position perpendicular to the surface is held constant. In such a setup, the measured differences in interaction strength can be interpreted e. g. as topography. In a more common setup, the tip is held at a constant interaction strength with respect to the surface by moving the piezo scanner accordingly at each point of the scan. This is called constant interaction mode, e. g. constant current for STM or constant force for AFM. Using constant current mode in STM corresponds to approaching if the tunneling current drops and retreating if the tunneling current rises. This is done with a feedback loop that feeds the measure of the interaction back into the piezo positioning. A computer is used to collect the data and for controlling the feedback loop at the same time.

When using a feedback loop, the voltage applied to the piezo element (perpendicular to the surface) reflects the topography with respect to the interaction used. Note that this varies depending on the technique used and on the sample under study. In STM, the level of constant tunneling current reflects a level of a given electron density, while in e. g. contact mode AFM this can be the level of mechanical contact between tip and surface.

The invention of STM was published in 1982[7, 8], and was honored with a Nobel Prize for Binnig and Rohrer just a few years later in 1986. Already 1985, the first AFM was implemented as a next step after the

STM by Binnig, Quate and Gerber[6]. Since then, a lot of effort was dedicated to improving AFM, introducing new measuring techniques that allow to measure not only the force between tip and surface, but also e. g. currents, work function and magnetic interactions, in most cases in addition to the force. In the following, we will discuss these techniques in more detail.

2.4.1 *Scanning Tunneling Microscopy*

Using the tunneling current between a tip and a surface is a relatively easy way to image conducting surfaces. The tunneling current I can be given as:

$$I \propto U\rho e^{-2\lambda d} \quad \text{with} \quad \lambda \approx \frac{\sqrt{2mW}}{\hbar} \tag{3}$$

The tunneling current is proportional to the applied voltage U and the local density of states close to the Fermi level ρ. It depends exponentially on the distance between tip and sample d. In good approximation, λ is a constant depending on the mass of the electron m and the work function W, $\hbar$ denotes the reduced Planck constant.

As the tunneling current depends exponentially on the distance between tip and surface, this technique is very sensitive to topographical changes. A small change of about $0.1\,nm$ in distance can easily lead to a change by an order of magnitude in the tunneling current. This is at the same time the main limitation of STM, as it is not possible to image non conducting surfaces.

The STM tip can be used to move atoms[11, 15] or molecules[16], and was shown to induce chemical reactions upon exciting a molecule by applying a voltage pulse[1, 22]. This principle was extended to the synthesis of a polymer from its ordered monomers induced by STM[37, 38].

Magnetic tips were used to spin polarize the tunneling current, allowing to investigate the local density of states with respect to their spin[10, 48].

2.4.2 *Atomic Force Microscopy - Contact Mode*

The first attempts to build an instrument that is capable of overcoming STMs limitation to conducting surfaces resulted in contact mode AFM. In the most common setup, a tip is mounted to the piezo ele-

ment via a flexible beam, as shown in Figure 5. When bringing the tip close to a surface, the forces acting on it will deflect the beam. This deflection is proportional to the force (to a good approximation). Most commonly, the deflection is measured by a laser beam directed at the end of the cantilever. Other approaches to measure the deflection of the cantilever like interferometry or using a STM on top allow a good performance, too[42]. However, we will focus on the setup with a reflected laser beam here: The reflection of the laser can be focused onto a Position Sensitive Device (PSD) far away from the cantilever, thus allowing to measure even small deflections of the cantilever at the PSD. The force calculated from this deflection can be used as a feedback to regulate the distance between tip and sample. In addition, the lateral deflection of the laser gives information about the friction forces acting on the tip.

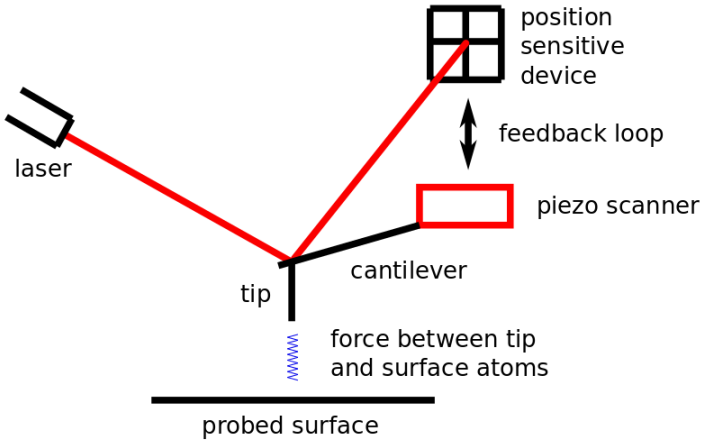

Figure 5 – A sketch of the working principle of AFM

One of the main disadvantages in contact mode AFM lies in the strength of the interactions between tip and surface. The sample can easily be changed by the influence of the tip, and vice versa the tip can get blunt when measuring with too large forces. Nevertheless, the technique was proven to allow for atomic resolution with a suited setup[5]. Moreover, different techniques of contact mode AFM were implemented, depending on the physical property in question, such as tribological behavior or electrical conductivity. The latter leads to the so called Conductive Atomic Force Microscopy (CAFM), which will be presented in more detail later (see Section 2.4.4).

2.4.3 *Atomic Force Microscopy - Non-contact Mode*

Non-contact mode AFM is a method were the tip is not in physical contact with the probed surface. In order to achieve this, the cantilever is resonated close to its resonance frequency. Typically, the resonance amplitude is in the order of 100 nm with a cantilever setup. Resonance frequencies are about 200 kHz. Compared to cantilevers used in contact mode AFM, an about two orders of magnitude higher stiffness (of about 50 $N\,m^{-1}$) is desired in order to prevent the tip from snapping into contact with the surface. When long range (e. g. van der Waals) forces start to act on the tip, they affect the resonance frequency of the cantilever, allowing to derive forces from the measure of resonance frequency shifts, given that the stiffness of the cantilever is known.

The shift of the frequency can be measured in two distinct ways: either the driving frequency is held constant, and a shift of the resonance peak is detected via its influence on the resonance amplitude, or the amplitude is held constant with a phase locked loop, and the changes in driving frequency is used as direct measure of the shift. The first method is called Amplitude Modulation AFM (AM AFM), the latter Frequency Modulation AFM (FM AFM).

2.4.4 *Conductive Atomic Force Microscopy*

As noted above, CAFM is a common extension of contact mode AFM, where conductive tips are used in a contact mode AFM. It was first introduced by Murrell et al in 1993[34]. Conductive tips can be either intrinsically conductive or coated with a conducting layer[17]. Intrinsically conductive tips - like doped silicon - often are subject to an oxidation reaction, making them better suited for the use in vacuum, as the oxides are usually non-conductors. In this study we used PtIr-coated tips, which are resistant to oxidation and reasonably resistant to wear, but have larger tip radii of about 25 nm instead of the 10 nm for uncoated tips. Thus, the spatial resolution is limited compared to both contact and non-contact AFM or STM. More recently, graphene coated CAFM tips have been developed[28], which are more resistant to both high currents and mechanical wear compared to metal coated tips, while also preserving small tip radii[25].

Using such a tip, the local current can be mapped by applying a bias voltage between tip and sample. In contrast to STM, the tech-

nique can be used on surfaces that are not conductive, or where only parts of the structures are conductive, as the current is not needed as a feedback in the scanning process. Thus, the CAFM setup can shed light on the conductivity and charge transport in semiconductor architectures[24].

2.4.5 *Kelvin Probe Force Microscopy*

Kelvin Probe Force Microscopy (KPFM) is an extension of non-contact AFM allowing to map the work function of a surface[31, 36]. During a KPFM scan, each line is scanned twice. The first scan of each line is a standard non-contact AFM scan in order to measure the topography. This data is used during the second scan of the same line, where the piezo controls the tip position such that it has a constant distance to the surface at all times. Simultaneously, an alternating voltage bias is applied between tip and sample.

2.4.6 *qPlus*

A relatively recent invention called qPlus aims at the combination of AFM and STM in a single tip. A conducting tip is mounted to a quartz tuning fork as commonly used in watches[19]. The resonance frequency of quartz tuning forks can be controlled precisely, and in the commercial mass market product it is usually fabricated with a resonance frequency of 32 768 Hz. This is favorable for digital clocks, as it is a power of two (2^15) and allows a simple bit counting resulting in a very precise measurement of a second.

The tuning fork itself is attached to a piezo with one of its prongs, as shown in Figure 6. With this setup, the tip can be resonated by driving the tuning fork. Due to one prong being fixed to the piezo element, and the mass added by the tip, the resonance frequency is typically in the order of 16 kHz to 20 kHz. Typically, the amplitude of the resonance is in the order of 1 nm to 10 nm, and thus much lower than in the more common cantilever setup[19]. With this setup, FM AFM is a much more sensitive application, especially when using the system in UHV.

Driving the tuning fork allows for the use of the instrument as a non-contact AFM. Using such a setup in AFM mode, the distance between tip and sample is comparable to the typical distances used in STM. Both the amplitude and the distance between tip and sample

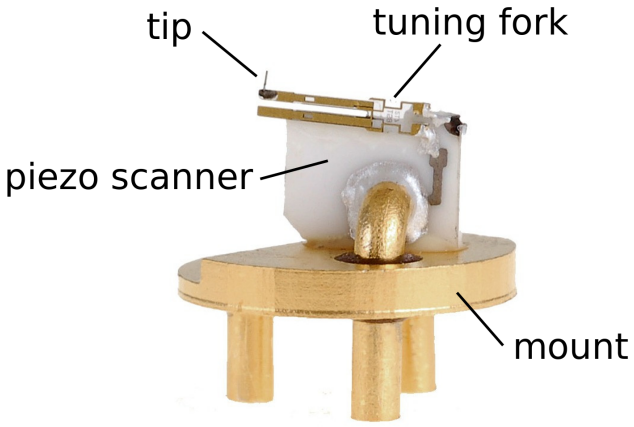

Figure 6 – A photography of a qPlus sensor by Omicron.

is rather low (about 1 nm to 10 nm) in comparison to AFM with a cantilever mount. This allows to measure the tunneling current while performing a AFM scan. Moreover, it enables to perform a STM scan while driving the tuning fork, simply by using the tunneling current as feedback instead of the frequency shift. This is called dynamic STM.

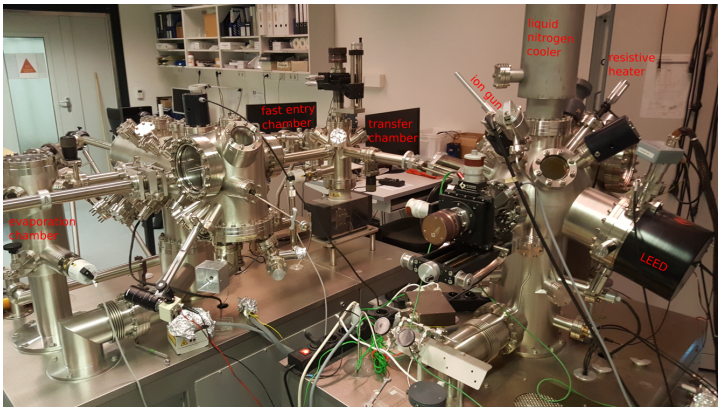

Figure 7 – A photography of the UHV setup in Freiburg.

The UHV-setup used in Freiburg is shown in Figure 7. It consists of two main chambers, a transfer chamber (smaller chamber in the background) and an evaporation chamber (smaller chamber on the left hand edge of the picture). Each main chamber contains a stage for STM measurements. In the left hand main chamber, AFM measurements with the traditional cantilever setup can be performed alternatively. The attached evaporation chamber allows evaporation of molecules through a crucible with a separated set of vacuum pumps. The right hand main chamber allows for alternative qPlus measure-

ments. A low energy electron diffraction (LEED) setup allows to check the crystallinity of samples, e. g. of graphene. An ion gun can be used to clean surfaces with argon ions. Samples can be heated via resistive heating using different contacting techniques. The right hand main chamber can be cooled using liquid nitrogen or helium, in order to reduce thermal noise during measurements. The transfer chamber allows to transfer samples between the main chambers. It also has a separate set of vacuum pumps and a fast entry chamber, allowing to introduce samples relatively quickly.

2.5 ORGANIC SEMICONDUCTORS

Most organic materials are insulators, but it is well known that organic materials can transport charges in certain circumstances. Charge transfer complexes were found to have semiconducting properties in the 1960s[26, 27]. The discovery of conductivity in conjugated polymers by Shirakawa, Heeger and MacDiarmid in 1977 earned them the Nobel prize in chemistry in 2000[21, 44]. In addition, small conjugated molecules have found to exhibit semiconducting properties as well. The basis of charge transport in all of these materials is the formation of π-bonds. Organic semiconductors are mainly based on carbon and hydrogen, where σ- and π-bonds form between the carbon atoms. The molecules can also contain other elements, most commonly sulfur, oxygen and nitrogen, which allows for a wide range of compounds with various properties, and an uncountable number of possible variations.

The formation of π orbitals is a consequence of the orbital hybridization. For carbon, the s and p orbitals are populated; at the ground state two electrons occupy the 1s orbital, another two the 2s orbital and one electron occupies each of two 2p orbitals. Slightly higher energy states are given from the superposition of the 2s orbital with any number of 2p orbitals. This process is called hybridization. The energy cost associated to the hybridization is overcompensated by the formation of σ- and π-bonds, and the lowest energy cost is given by σ-bonds in equivalent orbitals. When the carbon atom forms just two σ-bonds, as in e. g. acetylene, one of the 2p orbitals mixes with the 2s orbital. This is called sp-hybridization, which results in two sp orbitals used for (equivalent) σ-bonds and two lone p orbitals. In acetylene, both carbon atoms have two lone p orbitals, allowing them to form two π-bonds between them. Such a bond,

where a σ- and two π-bonds form between two atoms, is called a triple bond. When the 2s orbital hybridizes with two 2p orbitals (called sp^2-hybridization), the carbon atom can form three σ-bonds, and has one lone p orbital left for the formation of a π-bond. The ethylene molecule is the simplest example of two carbon atoms in sp^2 hybridization, forming a π-bond out of the two lone p orbitals. Such a bond is called double bond. Finally, a carbon atom can form four similar σ-bonds through sp^3-hybridization, like in ethane or methane.

As a consequence of the overlap of wave functions, π-bonds are delocalized. In a polymer like polyacetylene, where double bonds alternate with single bonds, the π-bonds are delocalized and can transfer charges along the backbone in the direction of the π-bonds. Charges can also be transferred to neighboring molecules. These processes are strongly dependent on the chemistry of the molecule and its orientation to its neighbors. It was found that crystallization can enhance the charge transfer in between molecules. As the transfer of electrons from one molecule to the next is associated with losses, well ordered packing reduces these losses due to both reduced distances and fewer displacements.

2.6 ORGANIC FIELD EFFECT TRANSISTORS

Transistors can be used as amplifiers and as electronic switches. As such, they can be used to form all forms of logic gates, being the foundation of modern computing. Here we will discuss the basic working principle and properties of transistors built from organic semiconducting materials, called Organic Field Effect Transistor (OFET)s.

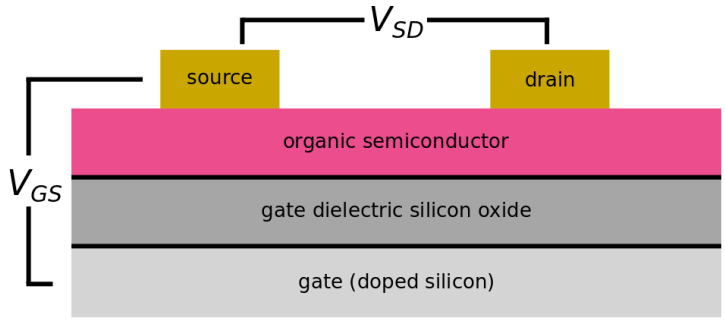

Figure 8 – A sketch of a top-contact bottom-gate OFET

A typical setup of such a OFET is shown in Figure 8. A FET contains three contacts, called source, drain and gate. The source and drain contacts are connected via a semiconductor, which is separated

from the gate via a dielectric. In principle, this configuration can be manufactured in many different ways. As manufacturing silicon wafers with a thermal oxide layer is well controlled and cheap, these are often used as gate and gate dielectric. The organic semiconductor can then be applied via surface coating methods, such as e. g. spin coating or drop casting. After any processing, e. g. crystallization of the film, source and drain contacts are applied, usually via physical vapor deposition. The configuration shown is called top-contact bottom-gate, and used in this study. Configurations where the organic semiconductor is applied after the source and drain contacts (called bottom-contact bottom-gate) are popular, too. In addition, it is possible to use other, even flexible substrates, and to apply the gate on top of the semiconductor. In this way, both bottom-contact top-gate and top-contact top-gate devices can be constructed.

Applying a voltage V_{GS} between gate and source electrodes results in an accumulation layer of electrons or holes in the organic semiconductor, depending on the sign of the applied voltage. Here, the organic semiconductor and the gate can be seen as a capacitor with the silicon oxide as dielectric. These charge carriers can be extracted through the drain contact by applying a voltage V_{SD} between source and drain.

As long as $V_{SD} \ll V_{GS}$, the accumulation layer connects both contacts and the charge carriers can be extracted through the drain, resulting in Ohmic behavior. Operating a FET under these conditions is called the linear regime. For larger V_{SD}, the region close to the drain is depleted from charge carriers. Here, a Space Charge Limited Current (SCLC) flows through the depleted region. When increasing V_{SD} further, the depleted region grows and the SCLC has to bridge a larger gap, which effectively limits the maximum current. Thus this operating regime is called saturation regime. This can be visualized when plotting the current I_{SD} between source and drain over V_{SD} as shown in Figure 9. Such a plot is called output characteristic. Plotting I_{SD} over V_{GS} is called transfer characteristic.

The mobility can be extracted from the following equation,

$$\mu_{sat} = \frac{2L}{WC} \left(\frac{\delta \sqrt{I_{SD}}}{\delta V_{GS}} \right)^2 \tag{4}$$

where L denotes the length of the channel (the distance between source and drain electrodes), W the width of the channel (the length

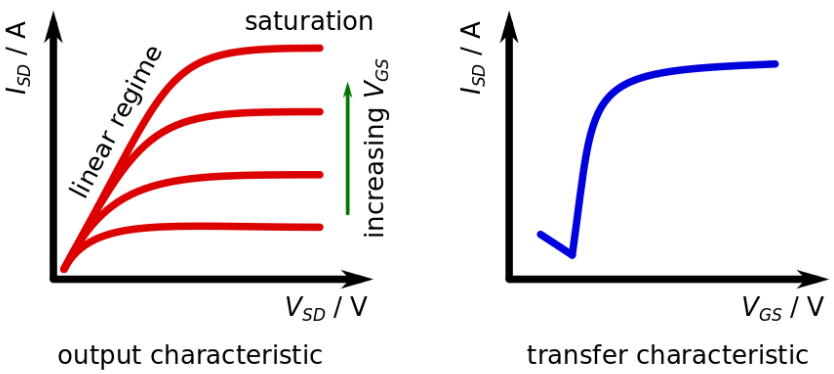

Figure 9 – Output and transfer characteristics of an ideal FET.

of the electrodes), and C the capacity of the dielectric between gate and semiconductor.

2.7 CHEMICAL SENSING

Chemical reactions and intermolecular interactions can influence the absorption and fluorescence spectra of molecules. This effect is used in optical chemical sensors, where a color change represents the presence of a specific concentration of a certain analyte molecule. The pH indicator paper strips are a well known example for this kind of a chemical sensor, here detecting hydronium or hydrogen ions. Depending on the interactions between analyte and detecting molecules, a wide range of molecules can be detected.

Another possibility is the application of a surface acoustic wave sensor, where an acoustic wave is generated in a thin polymer film and evaluated at another position. Changes in the response, such as amplitude, frequency, phase or travel time changes, can be attributed to changes to the film. In the case of a chemical sensor these changes are due the adsorption of a specific analyte molecule to the film - generally speaking other properties of the film such as viscosity or magnetization can be used for applications. The probability of a molecule adsorbing to a polymer film depends on the analyte-polymer interactions, which allow these sensors to exhibit specific responses to single target molecules, and thus allowing to identify a target analyte based on its calibrated response.

In 1981 it was found that when using Pd as a gate in a FET, the catalytic reactions of hydrogen introduces traps in the gate, effectively changing the gate voltage, which in turn can be measured in the FET[12]. This allows to measure the concentration of hydrogen in the gas surrounding the FET. Similarly, adsorption and chemical reactions in the channel of an OFET can be measured. Here, the analytes can exhibit specific responses, too. Such chemical sensors are usually called electronic nose[50]. Various applications from detection of diseases through analysis of breath odor[18, 46] to the quality control of groceries[49].

3

CRYSTAL GROWTH

In this chapter we will discuss the growth of crystals from thin 5TBT films on various substrates. The substrates employed during this thesis include silicon wafers with native and thermal oxide layers, and graphene grown from silicon carbide. Here, we examine the growth of 5TBT crystals on these substrates, starting with silicon wafers with a native oxide layer (with a thickness of about 2 nm). Subsequently we will investigate the surface structure with Atomic Force Microscopy (AFM), before discussing the growth mechanisms on silicon wafers with a thermal oxide layer (with a thickness of about 100 nm) and finally on graphene. We will discuss our finding about the influence of light on the crystallization process and the chapter ends with an investigation of the conductivity with Conductive Atomic Force Microscopy (CAFM).

3.1 GROWTH ON SILICON WAFERS WITH NATIVE OXIDE

For the study of crystal growth of 5TBT in thin films, commercial highly doped silicon wafers were used. These wafers are cut from a pure silicon crystal, and originally have no oxide layers. As silicon oxidizes under ambient conditions, an about 1 nm to 2 nm thick oxide layer forms when exposed to air. This so called native oxide layer passivates (protects) the underlying silicon from further oxidation. Wafers were consecutively cleaned in ultrasonic baths of water with soap, acetone and isopropanol for 15 min each.

Spin coating a solution of 5TBT in toluene onto these wafers leads to thin and homogeneous films. At a concentration of 0.0025 mg μl^{-1} and a spinning speed of 2000 min^{-1}, the resulting films have a thickness of about 10 nm. The thickness can be easily controlled by varying the spinning speed.

Samples were heated on a Linkam hot stage, allowing simultaneous observation by microscopy. This setup allows the direct observation of the film melting at 186 °C.

In order to crystallize a film, the sample is first heated slightly above the melting point. As can be seen in the temperature protocol

in Figure 10, the temperature is cooled down to a lower crystallization temperature and held there until crystals have been grown fully. Depending on the nucleation density and the crystal growth speed (which depend on the film thickness and the crystallization temperature), crystal growth takes 1 h to 48 h. Samples should be held in the dark during growth, as light influences the crystal growth. We will discuss this effect in more detail in Section 3.4.

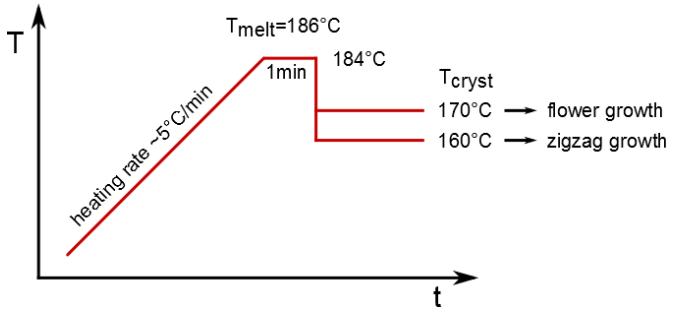

Figure 10 – A typical temperature protocol used to form crystals.

We observe different morphologies depending on the crystallization temperature. For crystallization temperatures around 180 °C, slightly below the melting temperature, the crystals grow into needles with a width of about 5 µm to 10 µm and a height of 0.1 µm to 2 µm; they can reach lengths of up to a 100 µm as shown in Figure 11

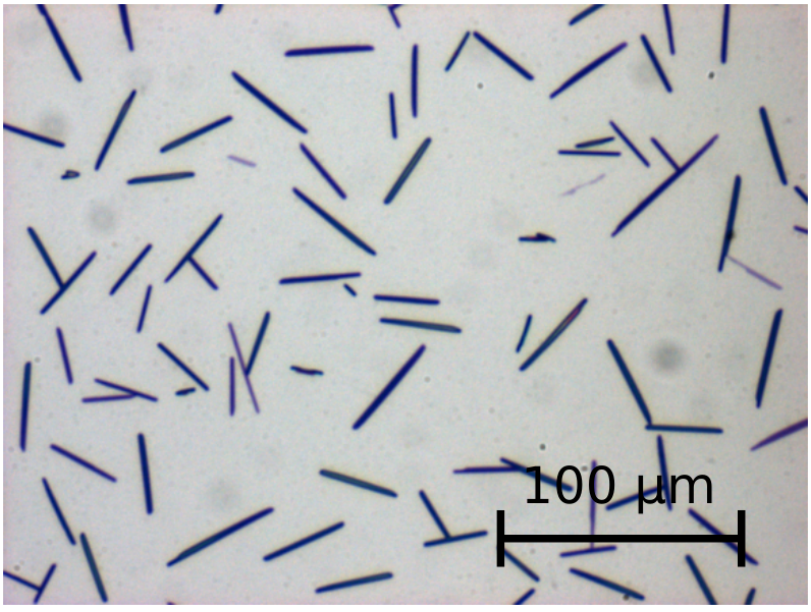

Figure 11 – Microscopy image of rod-like crystals grown from a thin film (2000 min^{-1}) crystallized at 180 °C.

These crystals resemble those grown in a previous study[32]. There, crystals were grown from 3TBT by cooling a solution in toluene slowly

below the point of saturation. A similar approach with 5TBT leads to aggregates without a clear morphology. Note that the 3TBT used in this study and the 5TBT used here differ not only in length, but also in the type of side chain (no branching in the case of 3TBT), which influences both solubility and crystallization. We suggest that the side chains play a crucial role during crystallization, both for the growth from solution and for the growth in a thin film. Similar behavior was observed during self-assembly with branched side chains[47].

For crystallization temperatures around 170 °C the crystals have a reduced height and are much wider, as can be seen in Figure 12. Changing the temperature influences the ratio of the growth speeds in different directions. Attaching a molecule to the side of the crystal instead of on the top becomes more likely with decreased temperatures. This change can be attributed to the difference in strength of the interaction between molecules depending on their orientation with respect to each other.

Similarly to the findings for 3TBT, when observing these crystals under crossed polarizers, they show strong birefringence. As the extinction position is aligned with the long axis of the crystals, the largest dipole moment is aligned with the fast growth axis of the crystal needles. Presumably, the dipole moment is caused by π-stacking interactions. Thus we conclude that, as expected, the fast growth is caused by the π-stacking interaction. This fits well to the observed differences in growth speed, as we can safely assume that the π-stacking interaction is stronger than the Van der Waals force based side chain interactions as well as the coupling between the end groups of the molecular backbone.

When crystallizing with even lower temperatures, the crystals start branching during growth, leading to single crystals covering a large area, as shown for a crystallization temperature of 160 °C in Figure 13. Each nucleus initiates growth through the film with a thickness of about the initial film thickness, stopping only when reaching the growth front initiated by other nuclei. With still lower crystallization temperature, the nucleation density rises, resulting in more nuclei and thus smaller and smaller single crystals.

A non-contact AFM image of a very thin crystal can be seen in Figure 14. The sample was grown from a film spin cast with a spinning speed of 2200 min^{-1} and a crystallization temperature of 170 °C. The resulting crystals are about 4 nm to 8 nm thick. We observe steps with

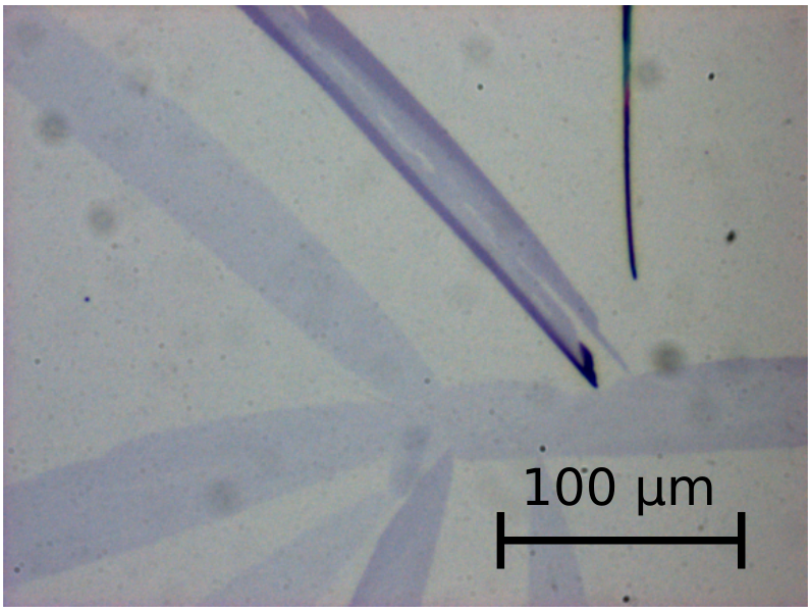

Figure 12 – Crystals grown from a thin film ($2000\,\mathrm{min}^{-1}$) at 170 °C are wider and less high, compared to the rod-like crystals.

a height of 2 nm on these crystals, and crystal heights are multiples of 2 nm.

The structure of the surface will be discussed in more detail in Section 3.1.1.

As the molecule is significantly planar and stiff, with a height of about 2 nm and a length of about 6 nm, the existence of crystals with a thickness of 4 nm suggests that the molecules are not standing upright.

Furthermore, the recurring height of the crystal steps of 2 nm fits well to the length of the molecules side chains, thus suggesting that the molecules are in an edge on configuration. This orientation of the molecules is consistent with the finding of large dipole moments along the fast growth direction, giving rise to the assumption of π-stacking along the fast growth direction, as discussed before.

The minimum height of crystals was found to be 4 nm, as shown in Figure 14, corresponding to a double layered crystal. Even when growing crystals from thinner films, no single layered crystals were found. Thus, we assume that the interaction between the side chains plays a crucial role in the nucleation process and crystal growth.

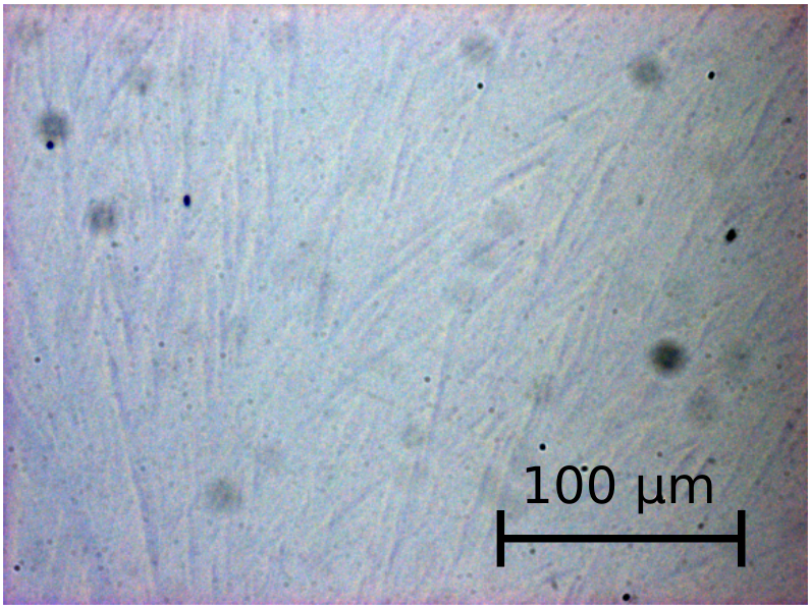

Figure 13 – Crystals grown from a thin film ($2000\,\mathrm{min}^{-1}$) at 170 °C are wider and less high, compared to the rod-like crystals.

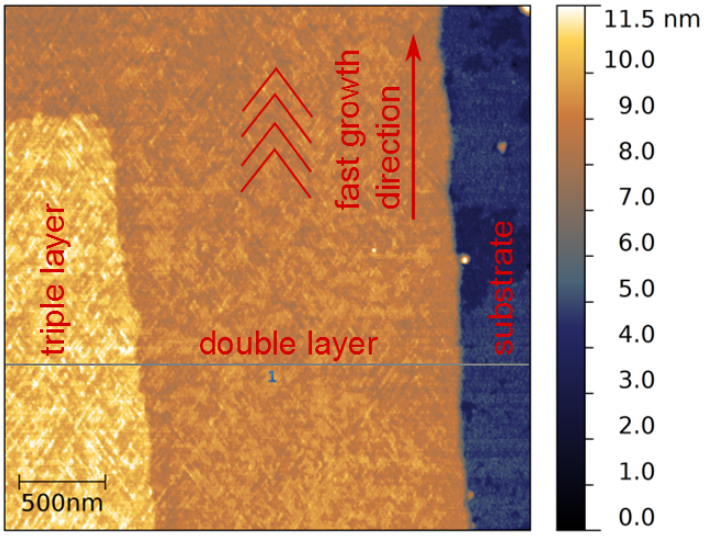

Figure 14 – An AFM image of a thin crystal. The surface structure is clearly visible and the step height indicates a double and triple layer.

3.1.1 *Surface structure characterization*

The surface of 5TBT crystals shows an intriguing structure. An AFM image of a 5TBT crystal grown on a silicon wafer with native oxide is shown in Figure 15. The crystal was grown at a crystallization temperature of 170 °C from a film spincast at 2000 min^{-1}. The surface structure is clearly visible, a quasi checkerboard pattern, with two types of domains, each one consisting of multiple parallel lines. The direction of fast crystal growth goes from bottom to top of the image (or vice versa). Note that the fast growth direction corresponds to the large dipole moment as seen in optical micrographs under crossed polarizers, and thus to the assumed π-stacking direction. With respect to the fast growth direction, the lines (marked in red) in the domains (marked in green) form an angle of 40° to each side.

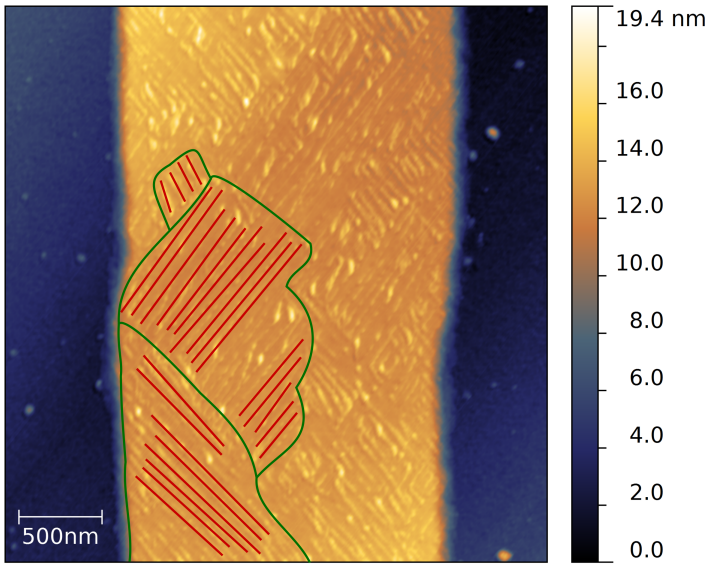

Figure 15 – An AFM image of a crystalline branch, with a clearly visible surface structure

This observation is consistent with other substrates and growth conditions, as it can be seen on silicon samples with and without thermal oxide, on crystals grown on graphene; and with various crystallization temperatures, independent of morphologies in the larger scale.

An apparent change in size, of both domains and the lines inside, can be related to the thickness of the crystals. The thicker the crystal, the larger the distance between lines gets, and the domains with identical orientation of the lines grows accordingly. In figure Figure 16, this dependency is shown to be linear over an order of magnitude.

We found that the distance between lines is independent of crystallization temperature. Both branched and elongated structures show the same distance between lines when comparing crystals of identical thickness. As we will discuss later in Section 3.2 and Section 3.3, the crystals grown on other surfaces than silicon with native oxide show differing morphologies. Nevertheless, the microscopic surface structure as observed by AFM stays the same. In addition, the distance between lines does not depend on the sample surface, but only on crystal thickness.

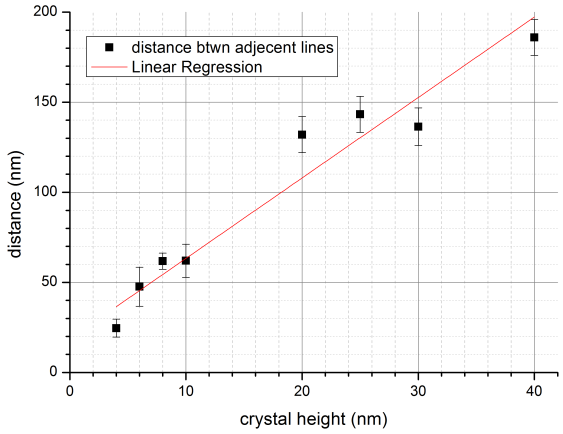

Figure 16 – Plot of the distance between lines on the surface structure over the corresponding height of the crystal.

Extrapolating the typical domain sizes to the thickness of rod-like crystals, which can reach a thickness between 100 nm and 1 µm, one would expect domains exceeding the lateral size of such crystals by at least an order of magnitude. Indeed, no domains can be observed in AFM scans of the surface of rod-like crystals, as shown in Figure 17. While the structure seems to have changed significantly, as neither the lines nor the domains can be found here, we suggest that the origin of the structure is the same. The lines as seen before spread out very far and they seem to turn to steps, forming edges at the side of the crystal rod. A second orientation, even though not aligned in a 40° angle here, can be seen in the phase image.

In Figure 18 we show how the surface structure transitions through different thicknesses. On this sample, initially the temperature was held at 180 °C for a few minutes. During this time, the higher, bottom part of the image has grown (as marked in green and yellow). Then, as we reduced the temperature to 160 °C gradually, the crystal starts to broaden and to branch along its growth (marked by a red arrow).

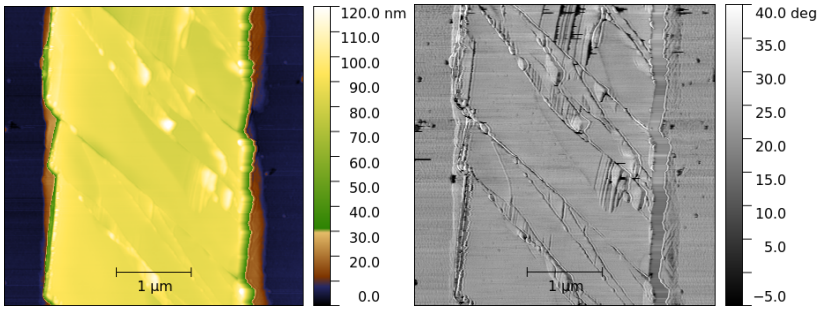

(a) Topographic non contact AFM image

(b) Corresponding phase image

Figure 17 – The surface structure of a rod-like crystal.

Eventually, it crystallizes in a branching fashion as seen before for a stable temperature of 160 °C (as marked in brown colors). Here, the dependency of both the surface structure and the crystal thickness on crystallization temperature can be seen in a single image.

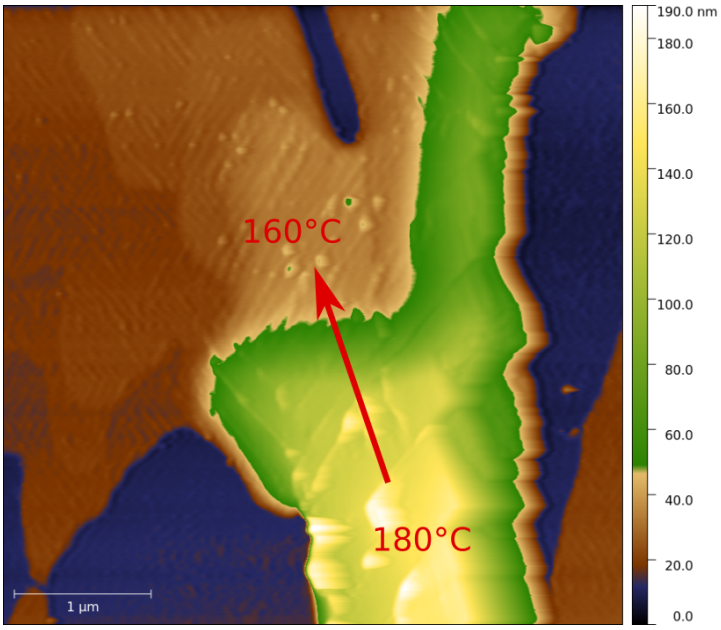

Figure 18 – An AFM scan taken on a sample where the temperature was changed from 180 °C to 160 °C during crystal growth.

3.1.2 *Solvent vapor annealing*

To further investigate the nature of the surface structure, samples as described above were exposed to solvent vapors. For Solvent Vapour Annealing (SVA), the samples are stored in a sealed glass container together with a reservoir of toluene for 18 h at room temperature. AFM

images of the samples were taken after the exposure, as depicted in Figure 19. Toluene was chosen as a good solvent for both benzene and thiophene, the molecules forming the backbone of 5TBT. In another experiment we used dodecane for SVA, as a good solvent for the side chain (2-ethyl-hexane) of 5TBT. As dodecane has a significantly higher boiling point, it does not sufficiently evaporate at room temperature to cause significant changes as seen for SVA with toluene. Hence, we stored the sealed glass container at a temperature of 50 °C. The resulting changes as observed with AFM are shown in Figure 20.

For both treatments, the surface structure changed significantly. The lines as seen before disappeared, and a different surface structuring emerged for both solvents. However, for toluene the surface structure still shows two major orientations, again with a 80° angle between them, symmetrically clasping around the fast growth axis. As before, we again observe domains where one of these orientations stays predominant. Next to the crystals, nanowire-like structures formed on the silicon oxide.

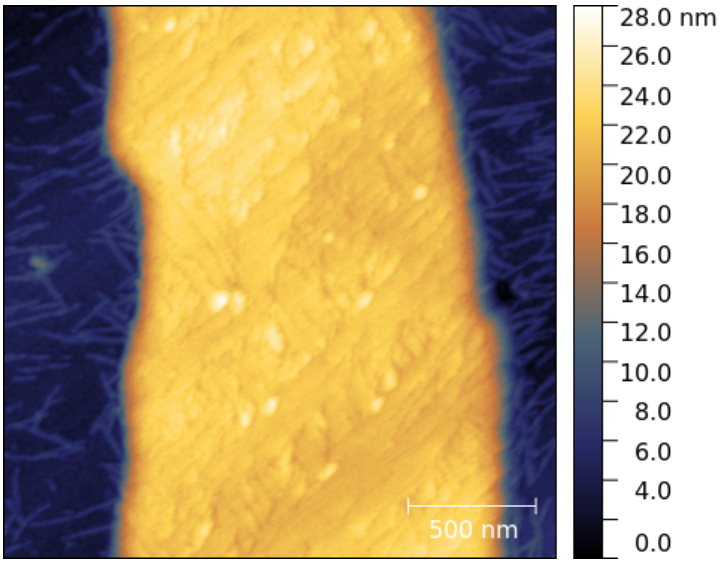

Figure 19 – An AFM scan after SVA with toluene. The fast growth axis is aligned from the bottom to the top of the image.

For dodecane, the situation is slightly different. While one of the orientations was preserved, in the domains where one would expect the other direction, lines along the fast growth axis emerged. Overall, the surface structure is more distorted, and when using even higher temperatures (e. g. 100 °C and 150 °C) during solvent vapor exposure to dodecane, the surface structure loses its order.

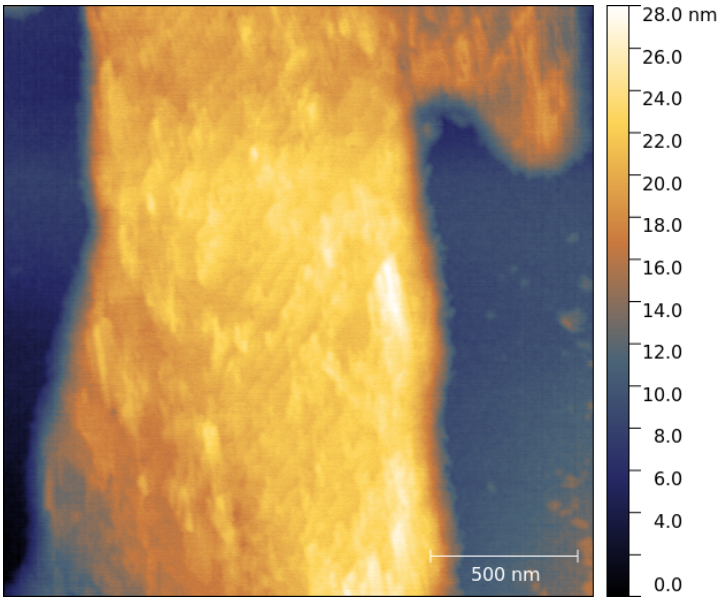

Figure 20 – An AFM scan after SVA with dodecane. The fast growth axis is aligned from the bottom to the top of the image.

The surface structure could be caused by surface stresses, growing through the crystal laterally. A possible explanation for these stresses can be found in the molecular arrangement. Different ways to stack 5TBT molecules are possible: Considering the stacking of molecules along the π-stacking direction, either 5TBT molecules stack with like aromatic rings on top of each other, or with unlike aromatic rings. In the first case, thiophene rings would stack on thiophene rings and benzene rings would stack on benzene rings. In the latter case, thiophene rings would stack on benzene rings and vice versa. However, due to the structure of the molecule, where always two thiophene rings stand between the respective benzene rings, two directions of such a stacking are possible. Such a stacking mechanism is shown in Figure 21. Using the unit cell parameters of 5TBT to determine the angle resulting from this stacking, we obtain an angle of 38°, in good agreement with the observed angle between lines and π-stacking direction of 40°. The changes from one stacking direction to another could be explained by stacking defects during crystal growth.

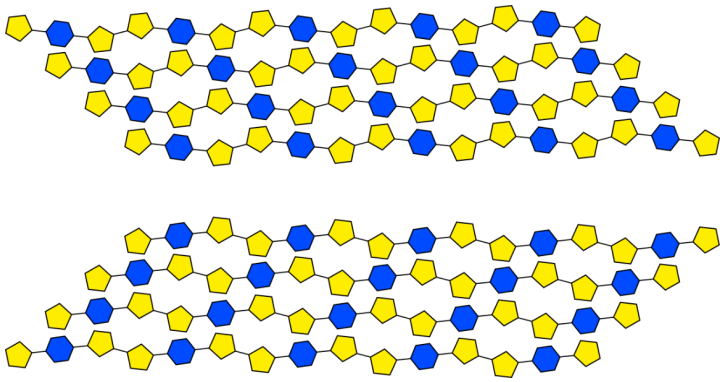

Figure 21 – Proposed stacking mechanism of 5TBT along the π-stacking direction. The π-stacking direction is thought to be from bottom to top. In the lower part of the sketch, stacking occurs to the right hand side, in the upper part of the sketch, stacking occurs to the left.

3.2 GROWTH ON SILICON WAFERS WITH THERMAL OXIDE

The branched structures formed on silicon wafers with native oxide are well suited for building field effect transistors, as the large scale single orientation allows for probing the charge transport along different directions. Especially the branched structures are promising candidates for the application of chemical sensing, as they cover large areas (even the complete sample) with a high density, thus increasing the sensitivity of the devices compared to needle like structures, as those have only a limited area exposed to the material.

As the application of a field effect transistor requires a gate, silicon wafers with native oxide are not the best choice. The native oxide layer has a thickness of about 2 nm, which cannot withstand gate voltages above 2 V. Growing similar structures on silicon wafers with thermal oxide poses the problem of dewetting, which usually inhibits crystallization. The attraction between a film and a substrate is dominated by van der Waals interactions, which themselves depend on the thickness of the oxide layer on silicon wafers[43]. With increasing thickness of the oxide layer, the long range attraction stemming from the pure silicon below the oxide decreases. For most organic molecules the attraction to silicon is much stronger than to the oxide layer, leading to a transition from wetting behavior to dewetting behavior with increasing oxide thickness. This effect can be observed for 5TBT. On silicon wafers with a thermal oxide layer (100 nm), spinodal dewetting occurs for films of 5TBT as soon as they are heated to the melting point at 186 °C. As the contact angle for 5TBT is very small,

the resulting structure consists of many homogeneously spaced and sized liquid pancakes.

Crystallizing those structures with a temperature of about 160 °C, a single crystal forms extending over many pancakes as seen in a microscopy image under crossed polarizers in Figure 22. Here, the fast growth axis extends diagonally from the bottom left to the top right of the image. Both sides of the image show the same area with different orientation of the crossed polarizers as depicted with red arrows. In the extinction position (left), only minor deviations of the optical axis can be seen by slightly illuminated spots. This proves that the crystal growth spreads through many pancakes without loosing its initial orientation.

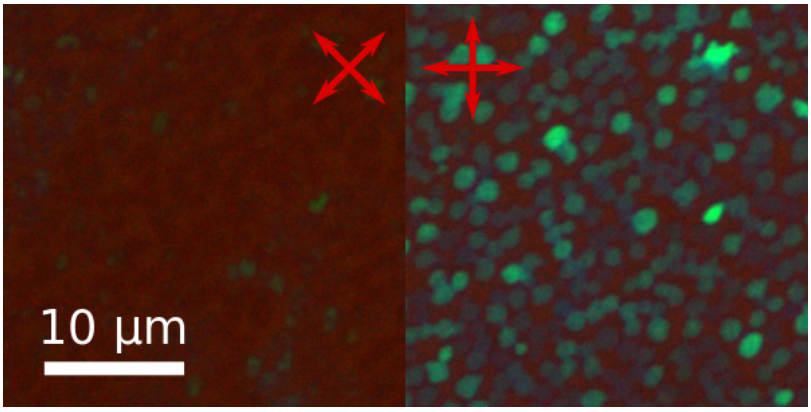

Figure 22 – Two optical micrographs of the same area under crossed polarizers with different orientation.

Figure 23 compares two samples grown at different crystallization temperatures, 164 °C and 172 °C, respectively. Note the large scale of the images, which were taken by stitching several large scale optical micrographs together. In both images, the crystals formed by some nuclei are visible, and the grain boundaries between those are marked by red lines. Two main differences can be seen when comparing those different crystallization temperatures. First, for higher crystallization temperature, the resulting crystals are larger. Secondly, in the high crystallization temperature we can observe region, where the surface is not covered by molecules. Instead, the edges of the crystals are higher (darker blue).

The first observation can be explained by the rise of nucleation probability with decreasing temperature. With lower temperature, thermal nucleation is more likely, thus each individual nucleus has less space to grow before reaching the growth front of another crystal. The second observation is explained by change of the ratio be-

tween π-stacking and vertical (along the backbone) growth speed of the crystals. In accordance with the previous observations on silicon wafers with native oxide, the ratio between the orthogonal growth speeds rises with increasing temperature. At some point, the growth orthogonal to the fast growth axis becomes slower than diffusion, resulting in high edges of the crystals and depletion zones in between them.

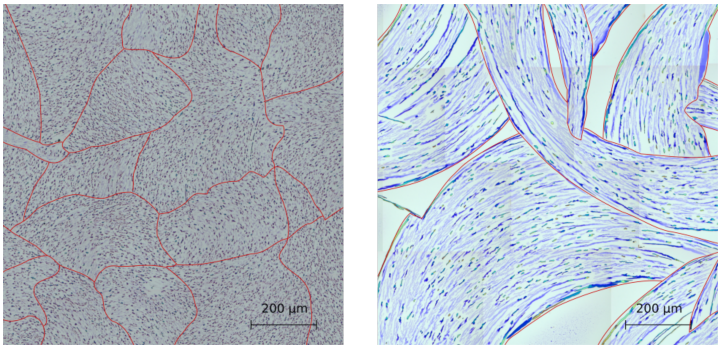

Figure 23 – Large scale optical micrographs of two samples grown at different crystallization temperatures: 164 °C to the left and 172 °C to the right, respectively.

Figure 24 shows a sketch of the time evolution for the growth of a single crystal through several pancakes. When a nucleus forms, it starts growing along the π-stacking direction much faster than vertically to the substrate (marked by green arrows to the left and right in Figure 24). Thus, the crystal spreads below a reservoir of molten molecules, which diffuse (red arrows) towards the growth front. Molecules may also diffuse over the surface from neighboring pancakes, allowing the bottom layers of the crystal to grow until eventually reaching neighboring pancakes. Hence, the crystal can grow through the next pancake rapidly, transferring the orientation of the initial nucleus. This process repeats into the next nearest neighbors until eventually ending when all pancakes on the sample are crystallized. Effectively creating large single crystals with unique orientation over hundreds of µm.

When reducing the crystallization temperature further, the nucleation density increases, and thus the size of the single crystals decreases. Upon quenching to room temperature quickly (e. g. by lifting the sample off the hot stage), the nucleation density is so high that each pancake forms its own nucleus. Also, the crystal growth speed increases so drastically (in relation to the speed of the diffusion) that crystals stay in the shape of the pancakes.

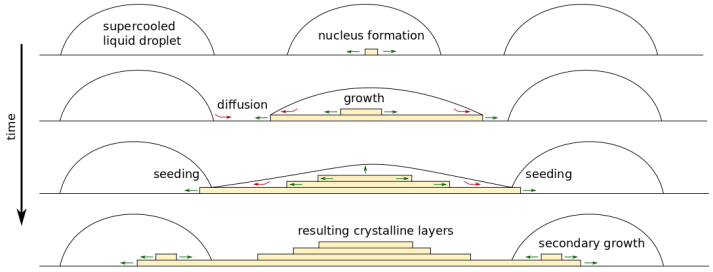

Figure 24 – Sketch of the droplet growth mechanism

3.3 GROWTH ON GRAPHENE

Using a conducting substrate for crystal growth allows to perform STM measurements, which in turn would provide additional information about the crystalline order, revealing the intrinsic stacking and may lead to better understanding of the surface structure. Graphene samples were prepared from polished silicon carbide plates. In silicon carbide, silicon and carbon atoms form alternating layers. When heating it to about 1250 °C in Ultra High Vacuum (UHV), the topmost silicon atoms evaporate, leaving a layer of carbon atoms that are only bonded to the carbon atoms below, creating a so called buffer layer. Upon further evaporation, the next layer of silicon atoms diffuses through the buffer layer and evaporates, too. Now, the second layer of carbon atoms bonds to the third, building the new buffer layer. In this case, the topmost carbon atoms form a layer of graphene without chemical bonds to the subsequent layers[4]. It stays attached to the surface through van der Waals forces. Graphene has been widely studied, and is well known for its potential applications as a tunable semiconductor[23, 29]. Here, graphene was used as a substrate to enable currents large enough for the use of Scanning Tunneling Microscopy (STM) and qPlus.

A first challenge to the growth of 5TBT crystals is the spin coating of the films. As the sample size of silicon carbide with graphene is limited to a maximum width of 2 mm in our setup, spin coating of homogeneous films is difficult. Droplets of solvent tend to stick to sample edges, resulting in considerably less homogeneous films close to said sample edges. This may affect the whole sample, when it is only 2 mm wide. However, even with poorly controlled film thickness, crystals can be grown from those films. As on silicon wafers with thermal oxide, 5TBT dewetts on graphene, resulting in an identical growth mechanism and similar morphologies.

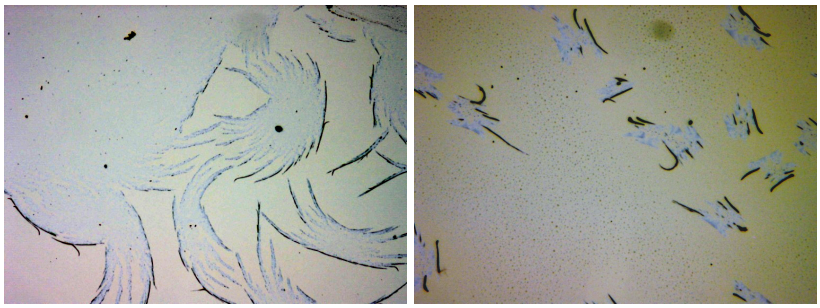

(a) Optical micrograph of the graphene sample, close to the edge of the sample.

(b) Optical micrograph taken far from the edge of the sample.

Figure 25

In Figure 25, two areas on one of the graphene samples are shown. As can be seen easily, the morphologies resemble those seen on silicon wafers with thermal oxide. In Figure 25 (a), the crystals grew via the growth mechanism proposed before. In Figure 25 (b), the crystals grew in a more rod-like fashion, while pancakes between the rods crystallized individually. This can be explained due to drastically different film thicknesses in the two areas, as the first image was taken closer to the edge of the sample, where the solvent droplet was pinned during spin coating.

Various AFM scans were taken at different spots on this graphene sample, showing the differences in morphology. Figure 26 shows scans from three different areas, one with small pancakes (a), one with larger pancakes (b), and one with a rod-like crystal (c). A zoom to the surface of the rod-like crystal is shown in (d). The surface structure has the same characteristics of lines and domains as presented before for silicon wafers with native oxide and thermal oxide. When considering the crystals thickness, the distances between adjacent lines on the surface fit well into the linear dependency as observed for crystals grown on native oxide. Thus, we conclude that the surface structure is independent of the substrate.

As graphene is a good conductor, STM can be performed on crystals grown on a graphene sample. We used qPlus in order to shed light on the connection between orientation of molecules and the surface structure. In principle, the AFM signal of qPlus gives information about the side chains of the molecules, while the STM signal shows the conjugation of the backbone. When measuring in pure STM mode, we achieved a stable signal. When exciting the tuning fork during an STM scan, molecules were moved by the tip. This can be seen in a

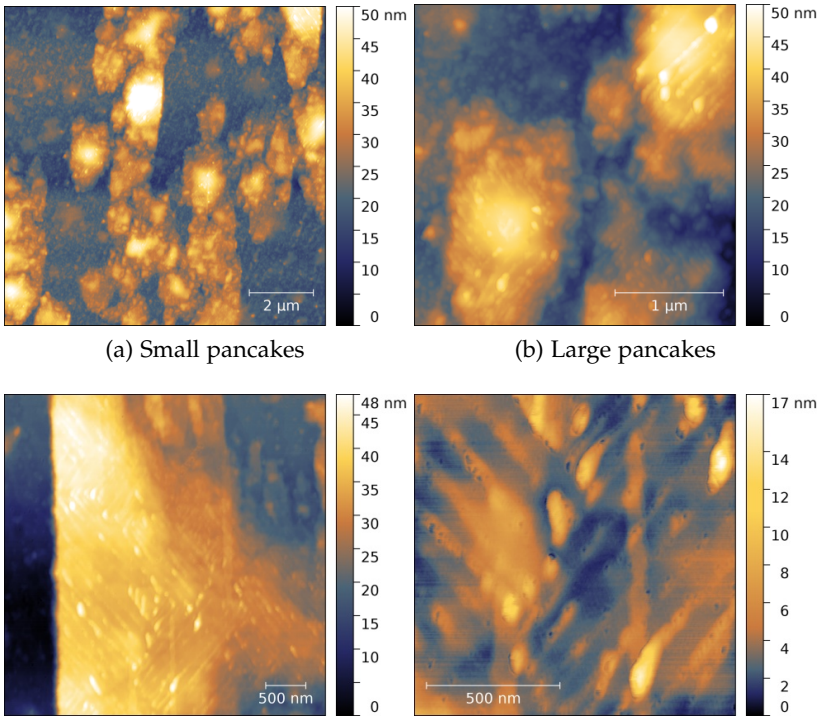

(a) Small pancakes

(b) Large pancakes

(c) Rod-like crystal

(d) Zoom to the surface of the rod-like crystal in (c)

Figure 26

scan in Figure 27. First, a scan was performed in dynamic STM mode. Afterwards, a second scan with larger scan area was performed in (pure) STM mode. The part of the image where the previous scan removed the molecules from the surface is clearly visible (and marked by a red square).

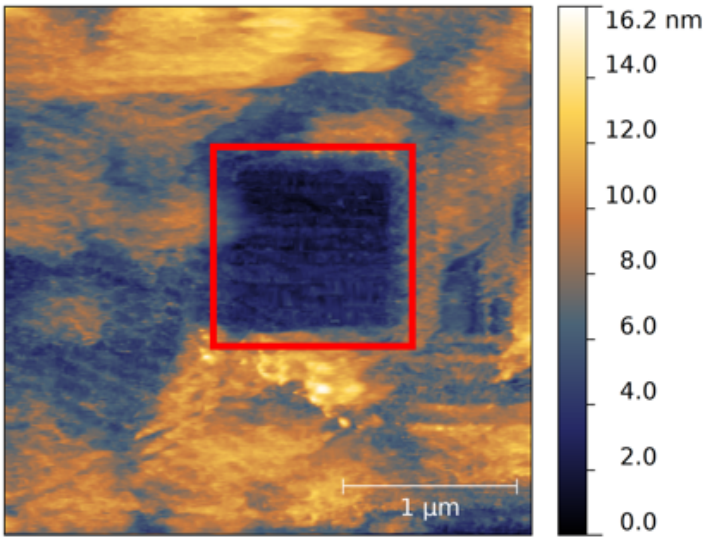

Figure 27 – qPlus image taken after a scan in the marked region. Molecules were removed from the surface due to the scanning.

3.4 LIGHT INFLUENCE ON THE CRYSTALLIZATION

We observed a strong inhibiting effect when shining light on the samples during crystal growth. It was observed to completely halt ongoing growth when shining intensive light (e. g. of the microscope) onto a growing crystal. Figure 28 shows the result of a crystal growth while the microscopes light source was focused onto a single spot on the sample. The sample was prepared by spin coating a film at $2000\,\mathrm{min}^{-1}$ on a silicon wafer with thermal oxide. After melting, it was held at 160 °C on a Linkam hot stage under a light microscope with the light source on for about 2 h. During the subsequent cooling to room temperature the light source was kept on, too.

After cooling, several images of the previously illuminated region were taken (with the same microscope), and stitched together to form a large area view as shown in Figure 28. The previously illuminated spot is marked with a red circle. As expected, the area that stayed in the dark crystallized as described before, forming a pattern of connected pancakes. On the other hand, the droplets in the illuminated area crystallized individually, during the final cooling to room temperature.

Right outside the border, a transition zone can be seen, where in many parts droplets in the dark also crystallized individually. This can be explained as nucleation density and growth speed are the limiting parameters. For each area, there is only a finite chance that a nucleus forms inside it. As the growth speed is limited, the crystals

closest to the illuminated area did not have sufficient time to crystallize up to the border in all the cases. This special situation allows us to investigate the differences between droplets that were exposed to light, and those that were not.

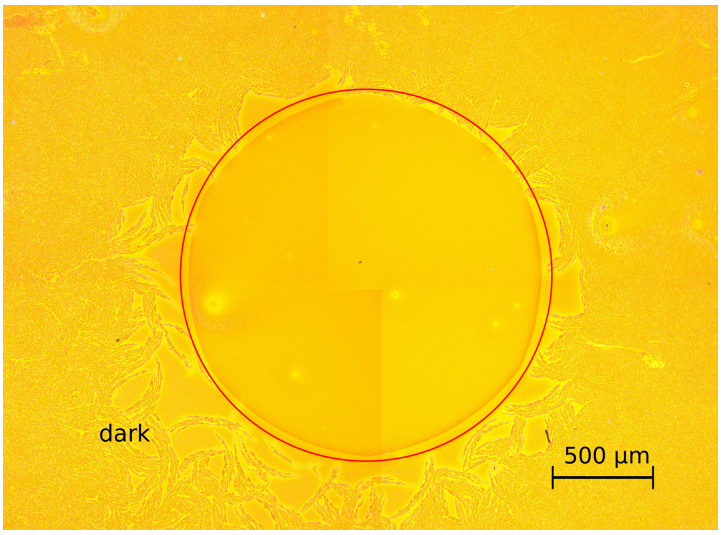

Figure 28 – Concatenation of optical micrographs of crystals grown over night. The light source of the microscope was switched on, illuminating the area indicated by the red circle.

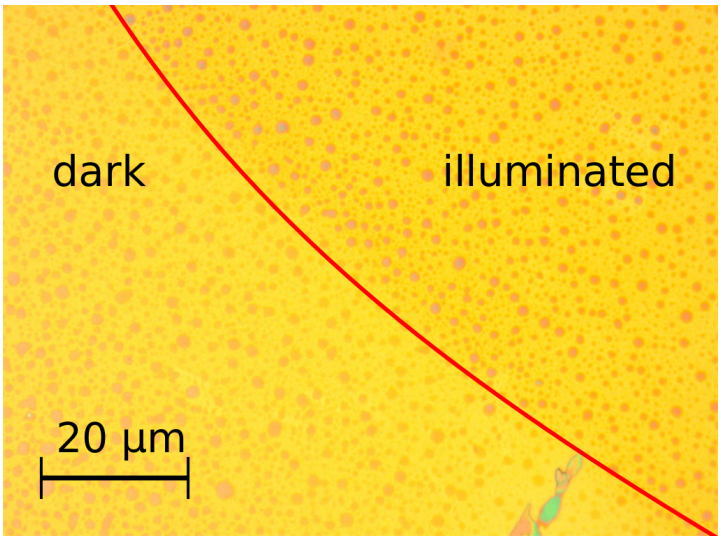

Figure 29 – A zoom to the edge between droplets under illumination (right side) and in the dark (left side).

A zoom to the border between both areas is shown in Figure 29. We can see two major differences: first, the droplets in the illuminated area are slightly larger and tend to be darker than the ones held in the dark, second, the color of the background (in between the droplets) is darker in the illuminated area than in the dark one.

The first observation indicates that the droplets in the illuminated region are slightly more spread out, and the different color indicates different heights. This can be confirmed by an AFM scan as shown in Figure 30. The scan shown here was taken right at the border between the two areas. Indeed, droplets on the illuminated side are less high, with a maximum height of 20 nm on the illuminated side compared to 28 nm on the dark side. In average, pancakes are 5 nm to 10 nm less high when illuminated. Thus, we can deduce that the light has an influence on the contact angle and the wettability, respectively.

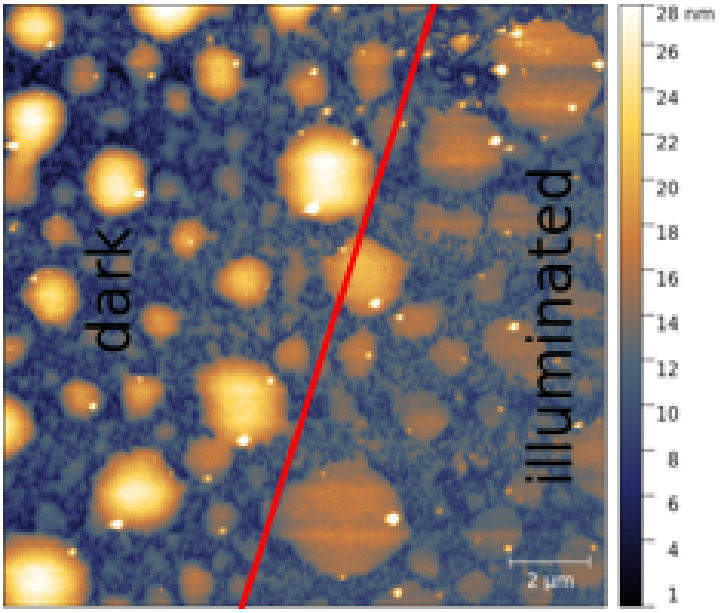

Figure 30 – Topographic AFM image of the border between illuminated and dark parts of the sample.

The second observation of differing background color in the two areas could be caused by an optical illusion, as the human perception judges color and contrast depending on the surrounding. Here, it is indeed a color difference, as can be shown by a RGB-value analysis as discussed in more detail in Section A.1 in the appendix.

As both the wettability and the color between the droplets changes, we assume that a layer of adsorbed molecules forms. We suggest that this layer gets disrupted by light, most likely due to a conformation change of the molecules when excited. Conformation changes upon excitation with light are well known for molecular switches [20] and even light powered molecular machines exist [2]. Such a conformation change could easily explain why molecules desorb under the influence of light. The presence or lack of such a layer can explain the color difference in the background. It would also influence the

wettability on the surface. Unfortunately, a more direct observation of the proposed layer is yet to find, as the resolution in our AFM set-up was not sufficient to prove the layer. Note here that we expect a height difference of only 0.05 nm for a single layer of molecules in flat on orientation, which is already smaller than the typical surface roughness of both the native and the thermal oxide.

We further suggest that the proposed absorption layer plays a crucial role in crystal growth, as crystal growth stops under the influence of light, and nucleation is fully inhibited. In addition, it could explain the observations previously described (see Section 3.4.1), where droplets shared the same orientation of surface structure (and thus molecular orientation) even though they were not visibly connected. A layer of adsorbed molecules may self assemble into highly ordered structures, as was e. g. shown for 3TBT. This order may transfer into the resulting crystal.

3.4.1 *Evidence for an underlying layer*

Figure 31 (a) shows the AFM scan of a crystal grown with the method described above, at a spin speed of 1800 min^{-1} and a crystallization temperature of 160 °C. Interestingly, while most of the pancakes have a visible connection to their neighbors and thus thousands of pancakes are connected to each other, the larger droplet to the bottom left seems to be connected to only two smaller pancakes to the top. Other instances of such separated pancakes where found in different occasions.

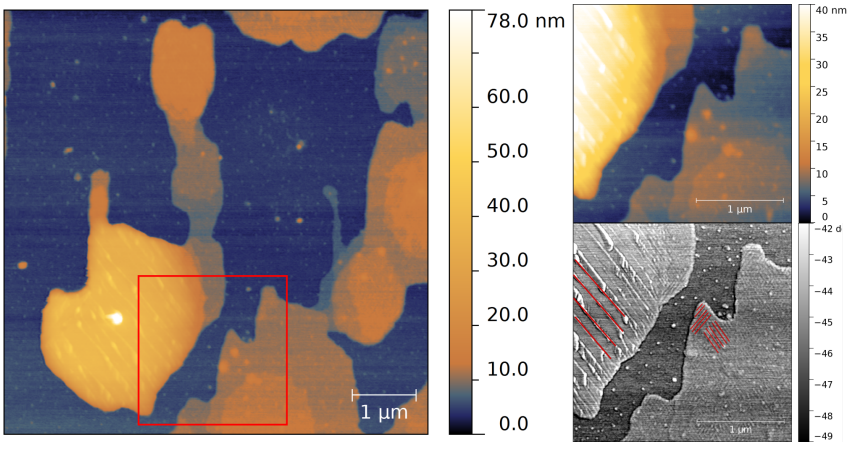

Figure 31 – qPlus image taken after a scan in the marked region. Molecules were removed from the surface due to the scanning.

In Figure 31 (b) we can see a zoom to the area marked by a red rectangle in (a). Figure 31 (c) shows the corresponding phase image, where the surface structure of the two pancakes is visible in more detail. Even though the pancakes seem to have no connection in the macroscopic scale, the orientation of the surface structure and thus the order of the molecules is well aligned. Considering the evidence for the underlying layer discussed in Section 3.4, we can further assume that the underlying layer transfers its own order into the crystallizing pancakes.

3.5 CONDUCTIVITY OF THE SAMPLES

In a first attempt to probe the conductivity of the samples, we used branched crystals grown on silicon wafers. Evaporation of gold lines through a mask allowed us to investigate the conductivity with CAFM. In this experiment, we contacted both the gold lines and the bottom side of the silicon wafers to the CAFM-base. In such a setup, source and base voltages are always the same, but it allows simple measurements of the conducting pathways. As we used native oxide layers, the base voltage was limited to about 2 V. With higher voltages, the oxide layer was not isolating anymore. However, these experiments confirmed that the crystals build conducting pathways, and that the current decreases according to the length of the pathway. Figure 32 shows a CAFM scan of such a sample. The electrode is directly to the right side of the image, but not shown here. As the electrodes are about 100 nm thick, scanning the electrodes quickly wears down the conducting tips and results in mostly distorted images, thus, the measurement of electrodes was avoided.

In Figure 32 (a) the topography of the branched crystals is shown. Note that the surface structure can not be resolved, as CAFM is a contact mode technique. The high interaction forces used in contact mode combined with the large tip radii used for CAFM reduce the resolution and increase the wear acting both on tip and sample significantly. The branches in this area were chosen with different lengths of the channel to the electrode. The branch to the right side is directly connected to the electrode. The middle branch has a relatively long path to the electrode via the top. The leftmost branch has a relatively short path to the electrode via the bottom.

Figure 32 (b) shows the corresponding current measured during the scan. It is clearly visible that the directly connected crystal shows

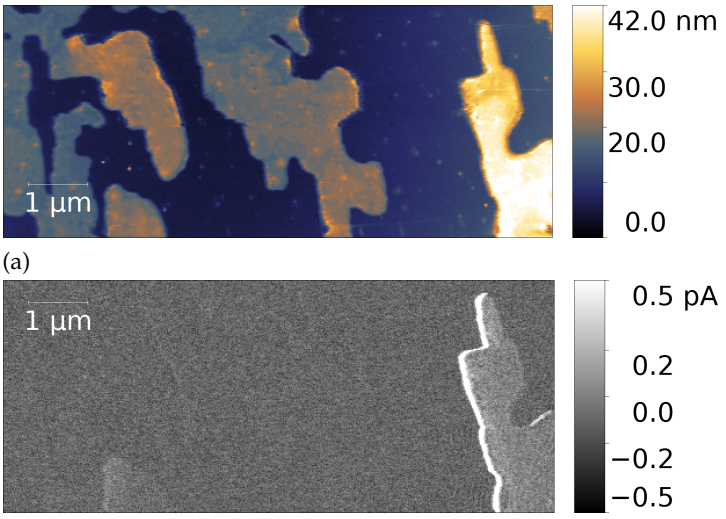

Figure 32 – Topographic (a) and current (b) CAFM image of a branched structure on a silicon wafer with native oxide layer. A gate and tip voltage of 2 V was applied. The crystal branch on the right side is directly connected to the electrode, the left branches are connected via a short path through branches to the bottom, the mid branch is connected via a considerably longer path to the top.

the highest currents. The bottom left crystal shows at least a little current, while due to the long pathway of the middle crystal no significant currents can be detected. Note also that the current is considerably larger on the edges of the crystal compared to the flat top of the crystal. This is in agreement with the assumed orientation of the molecules, as the side chains are expected to conduct much less than the π-stacked backbones. As the molecules are in an edge-on configuration and the highest mobilities are expected along the π-stacking axis and the backbone axis, while the side chains are expected to considerably hinder electron and hole transport, the electrons can be injected into the conducting channel best through the edges of the crystal, where no side chains block the pathway.

CAFM measurements in pancake structures yield similar results (compare Figure 33), however, here individual pancakes do not show reduced currents, even though they have no visible topographic connection, as can be seen for the pancake in the top middle of the image. This strongly suggests that the adsorbed layer enables the flow of electrons between the pancake structures.

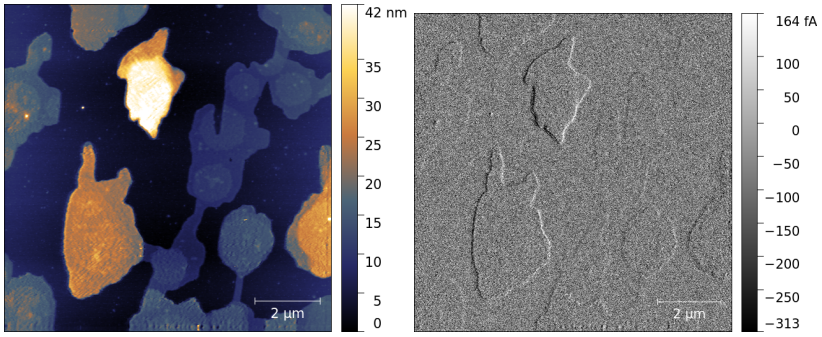

(a) (b)

Figure 33 – Topographic (a) and current (b) CAFM image of connected pancakes on a silicon wafer with thermal oxide layer.

4

FIELD EFFECT TRANSISTOR APPLICATION

In this chapter we present the fabrication and characterization of Field Effect Transistor (FET)s built from thin film crystals as described before. The resulting FETs can be used as chemical sensors for acetone, and finally we discuss experiments with regard to the detection of 2,4-Dinitrotoluene (DNT).

4.1 FIELD EFFECT TRANSISTOR FABRICATION

Samples with crystals grown on silicon wafers with thermal oxide are a good starting point for the fabrication of FETs. Therefore, silicon wafers were cleaned in soapy water, acetone and isopropanol for 15 min each, and subsequently introduced into the glove box. Spin coating and crystal growth was performed inside the glove box, in analogy to the experiments conducted outside previously. Evaporation of an injection layer of MoO and subsequently silver contacts through a mask results in a bottom gate top contact FET configuration. Samples were prepared in collaboration with the university of Strasbourg. The full process from spin coating, crystallization, evaporation of contacts and the characterization as described in the following section was performed under nitrogen atmosphere in a glove box. Contacts were evaporated in a high vacuum chamber directly connected to the glove box.

The size of the masks used ranged from 60 µm, 80 µm to 100 µm in channel length and from 21.88 mm, 29.17 mm to 36.46 mm in channel width, respectively. In Figure 34 an optical micrograph of such a FET built from a crystal grown at 160 °C is shown. The smallest mask was used here. In principle, different mobilities can be expected along different axis in organic semiconducting crystals. A higher mobility along the π-stacking direction is expected and well known for various molecules. Note that the size of the crystals at 160 °C is below the size of the FET, so that the channel consists of multiple crystals with random orientation. Given the size of the FETs used in this study, the measured mobility in this setup reflects an averaging over the mobilities along various directions.

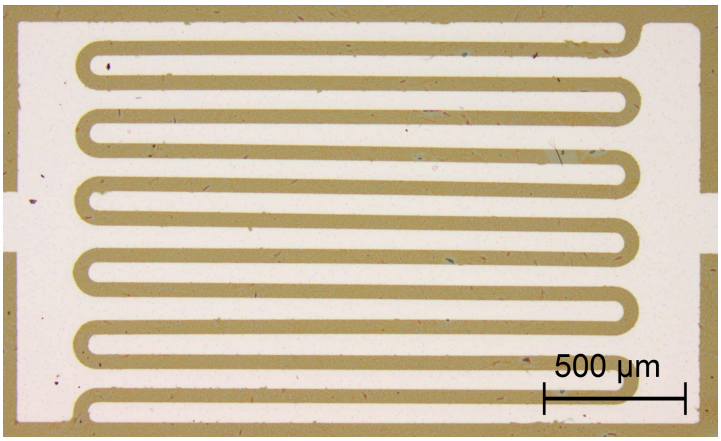

Figure 34 – Optical micrograph of a FET built by evaporation of silver on top of a crystal structure

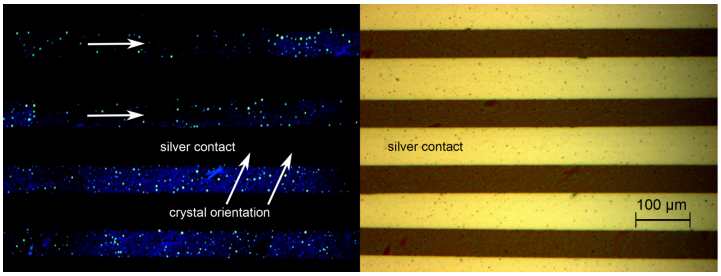

Figure 35 – A zoom to a part of a FET with a few channels. On the right, the channels can be seen in optical microscopy, on the left, the same area under crossed polarizers is shown. the luminescence of the crystals indicate their orientation, such that the size of individual crystals can be seen. Arrows indicate the local fast growth direction.

In this study we consider branched structures grown at 160 °C, as more narrow elongated structures do not fully cover the surface. Thus, FETs fabricated with such a morphology would need individual measurement of the channel length and width, as most of the surface are gets depleted of molecules, thus negating the advantage of this easily applicable technique.

In order to compare the mobility of the crystals, two reference samples were build: one with an amorphous film and one with separated, individually crystallized droplets. For the first, we spin cast a film at 2000 min^{-1}, and applied contacts without prior temperature treatment. In this case we expected a lower mobility, as crystallization is well known to enhance charge transport in systems with π-stacking. For the latter, we heated such a film to 186 °C and subsequently quickly quenched it to room temperature before the growth could spread across multiple droplets. For such a sample we had

initially expected to measure no current, as these droplets crystallize individually and do not form a pathway leading from one electrode to the other. However, in the next section we will present the observation of a current in such samples and discuss it in more detail.

4.2 FIELD EFFECT TRANSISTOR CHARACTERIZATION

Output and transfer characteristics of the obtained FETs were measured. Typical transfer and output characteristic are shown in Figure 36. The devices show only low leakage, a reasonably low contact resistance and well reproducible characteristics. Extracting the mobility from the transfer characteristics yields values from $1.0 \times 10^{-4}\,\mathrm{cm^2\,V^{-1}\,s^{-1}}$ to $4.0 \times 10^{-4}\,\mathrm{cm^2\,V^{-1}\,s^{-1}}$, depending on the device. Slight differences between the devices are expected for several reasons: the orientation of the crystals are not controlled in the setup, the thermal oxide layers are not perfectly homogeneous in thickness, and the evaporation of injection layer and silver contacts do not always yield the same contact resistance.

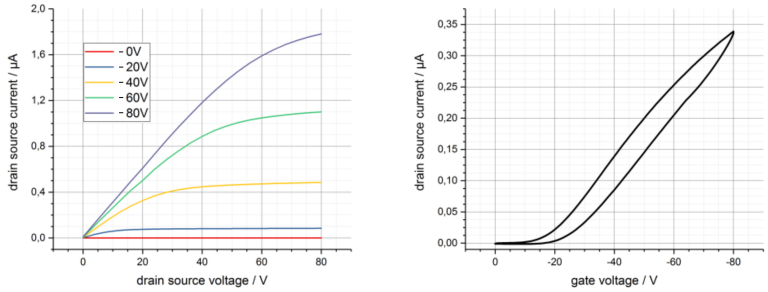

Figure 36 – Typical output and transfer characteristics of a FET as obtained by evaporation of contacts onto crystals grown at 160 °C.

The reference samples with an untreated, thus amorphous thin film show a mobility reduced by two orders of magnitude, consistent with the theory that order enhances charge transport in systems exhibiting π-stacking. Their output and transfer characteristics are considerably less stable.

Surprisingly, the devices that have no visible connection, as the pancakes grew individually through rapid cooling, show a well defined FET characteristic as well. Interestingly, the mobility of these devices is in between the amorphous reference and the crystalline devices, ranging from $1.0 \times 10^{-3}\,\mathrm{cm^2\,V^{-1}\,s^{-1}}$ to $4.0 \times 10^{-3}\,\mathrm{cm^2\,V^{-1}\,s^{-1}}$.

We assume that this effect can be attributed to the previously suggested surface layer of adsorbed molecules (compare Section 3.4). As we proposed before, we assume that this layer self assembles into a highly ordered structure, giving rise to nucleation and growth with a related order. This explains well why these extremely thin films show a higher mobility than the amorphous thin film devices.

Experiments described in this section were performed in a glove box under nitrogen atmosphere. Samples were removed after the measurement and exposed to ambient air for a month, and reintroduced and measured again for comparison. Degradation was unexpectedly low with a loss of about 10%.

4.3 CHEMICAL SENSING

In order to measure the capabilities of TBT to detect acetone and DNT, we used a chemical sensing setup in Strasbourg. The setup is shown in Figure 37.

The chemical sensor testing setup has two chambers, the Detector Chamber (DC), where the Organic Field Effect Transistor (OFET)s can be placed and their output and transfer characteristics can be measured, and a Analyte Chamber (AC) for introducing the analyte molecules into the gas flow.

Two Mass Flow Controller (MFC) allow the controlled flow of nitrogen through the chambers. The flow leads through the AC first, where the analyte molecules evaporate, and thereafter to the DC, where the detection of the OFETs can be evaluated.

Experiments are conducted in the following manner: Transfer characteristics of an OFET are measured at various gate voltages, scanning over the range of $-60\,V$ to $60\,V$ in steps of $10\,V$. This procedure minimizes saturation effects. The highest measured current of each cycle is then tracked over time. Usually this is the current at highest V_ds and highest V_g, only differing in case a measurement suffered from outside influences. Exposure to analyte molecules results in a change (usually a drop) of this current.

Figure 38 shows the detection of acetone with a 5TBT OFET built from a crystalline structure grown at $160\,°C$ as described before. The sample was measured in the DC-chamber with a constant nitrogen flow. During this first section of the measurement the maximum current slowly declines due to saturation effects. After changing the flow from pure nitrogen to a flow carrying acetone with the same flow rate,

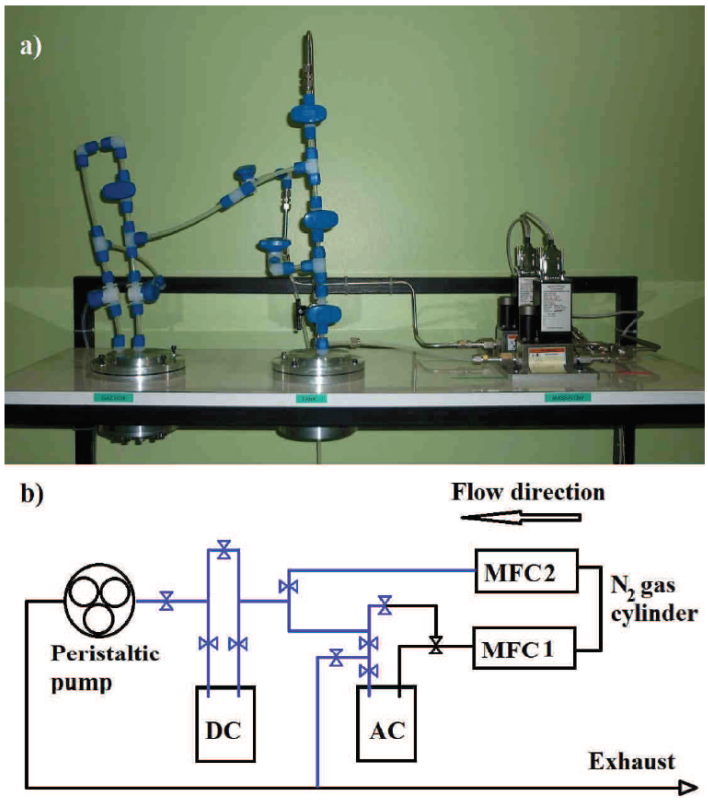

Figure 37 – Setup for measuring the sensitivity of FETs to chemical vapors, taken from reference

the maximum current drops exponentially, as molecules diffuse and attach to the conducting channel. After switching back to the pure nitrogen flow, the maximum current recovers partially. This may be due to the influence of the gas molecules on the surface structure. Due to time constraints, the surface structure was not investigated after the exposure to acetone, but drastic changes of the surface structure are known from other solvents, namely toluene and dodecane (see Section 3.1.1). Similar changes to the surface structure can be expected from acetone, as it also dissolves 5TBT to some degree. Such changes in surface structure could drastically influence the mobility of the crystal.

Detection of acetone by a FET built from a droplet type crystallization is shown in Figure 40. Here, the sample was quenched to room temperature rapidly after melting the film, resulting in apparently separated crystalline droplets, each with it's own nucleation and thus orientation. As the mobility in these samples is drastically lower, and the overall quality of the FET is worse, reliable results have been obtained for a smaller gate voltage range of $-40\,V$ to $40\,V$ only. Thus, the saturation effects are clearly more pronounced, as can be seen in

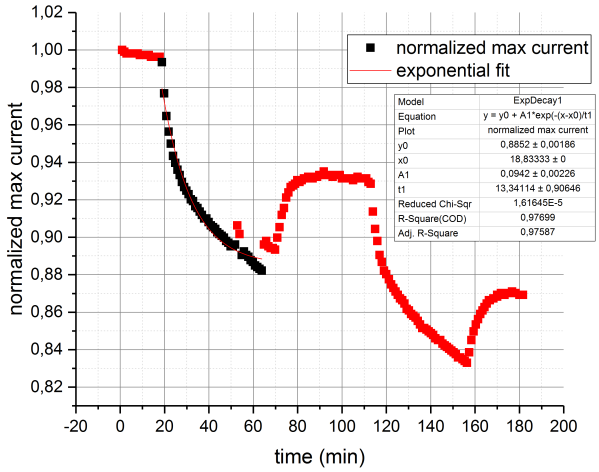

Figure 38 – Measurement of the maximum current flowing through a FET on a carpet type structure during exposure to acetone

the first 15 min of the experiment. Nevertheless, it clearly shows that the detection mechanism for acetone is independent of the morphology of the sample.

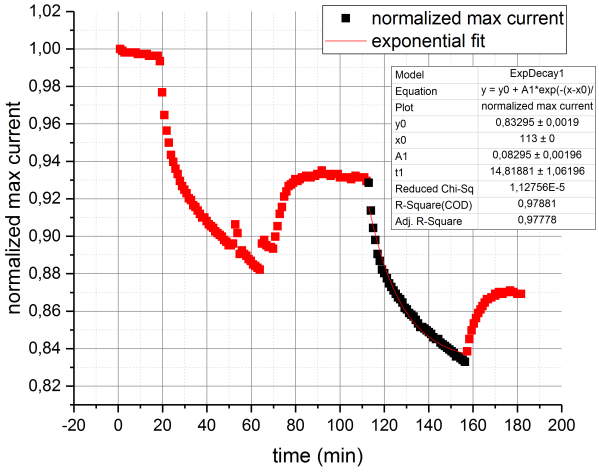

Figure 39 – A second exposure

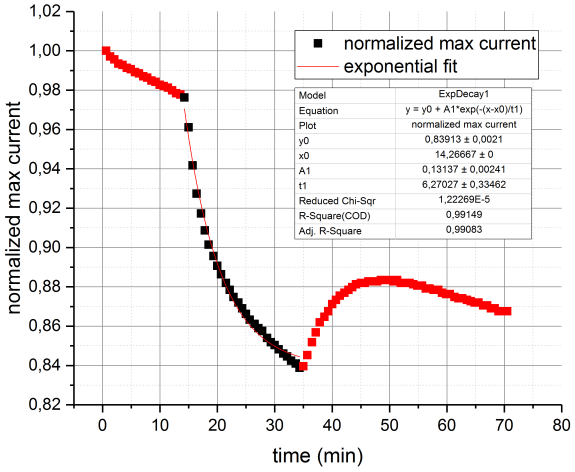

Figure 40 – Measurement of the maximum current flowing through a FET on a droplet type structure during exposure to acetone

5

OUTLOOK

This thesis has open up new questions that were not yet addressed. The most promising prediction from the observations for 5TBT is that similar, π-stacking molecules exhibit a similar growth mechanism after dewetting. Such an experiment could be performed with a variety of differing chemical structures, in order to see similarities between molecules and also limitations to this type of growth. Therefore, various lengths of TBT, different side chains and also different backbones (like e. g.Poly(3-hexylthiophene-2,5-diyl) (P3HT)) could be probed.

Unfortunately, the exact crystal structure could not be described fully in the time limits of this thesis, especially due to the instability of molecules when scanned with qPlus. Low temperature measurements with qPlus may yield better results. In addition to qPlus, a x-ray study could reveal the crystal structure, too.

Now, as the growth mechanism and preparation conditions are known, we set the foundation for further experiments. Expecting higher degrees of order with higher crystallization temperatures, a series of mobility measurements with differing crystallization temperatures could lead to further insight about the relationship between order and mobility. In addition, as we reached ordered structures in the μm-range, constructing Field Effect Transistor (FET)s with a single orientation throughout the whole channel seem feasible with a slightly more sophisticated application of the evaporation masks. This would allow a measure of the mobility as a function of the angle between π-stacking and channel, which by itself is an interesting question, not just for 5TBT but for π-stacking molecules in general.

Another promising set-up for an experiment would be to perform Kelvin Probe Force Microscopy (KPFM) on a running device while exposing it to analyte molecules (acetone, 2,4-Dinitrotoluene (DNT)). KPFM allows to visualize areas of differing work function and trapped surface charges. Thus, the positions where analyte molecules interact with the channel could be revealed. For example, the analyte channel interaction may be restricted to step edges or specific features on the surface structure of the crystals.

A

APPENDIX

A.1 OPTICAL ILLUSION

As mentioned in Section 3.4, human color perception depends on the surrounding. This may be applicable to Figure 29, as the color of the foreground (droplets) differs between the dark and illuminated regions, while the color of the background seems to change, too. This change could in principle be caused by an optical illusion similar to the Chubb illusion shown in Figure 41, where the background can influence the perception of the foreground. In this image, the circular central areas on the left and right are fully identical, but appear to be different due to the differences in the surrounding[14]. Knowing about optical illusions like this, one is left unsure about the true colors and ones own perception when watching Figure 29.

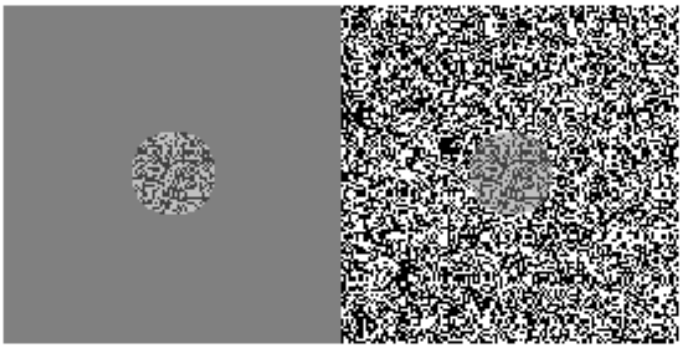

Figure 41 – The Chubb illusion, showing the same circular area in different context. The human eye takes the context into account and misinterprets the central areas as different.

In order to prove that no similar effect is responsible for the perceived differences in Figure 29, Figure 42 shows two slightly modified versions of the initial image. In Figure 42a, similar colors to a pixel in the background of the dark region were selected by the color selection tool available in the image manipulation program gimp. This tool selects all pixels in the image based on similar RGB values. Subsequently, their color was replaced by white in order to visualize which pixels indeed share a similar color. The same for similar colors in the illuminated region is shown in Figure 42b. Thus indeed not only the

color of the droplets but also the color of the background changes between dark and illuminated areas. An optical illusion can be excluded.

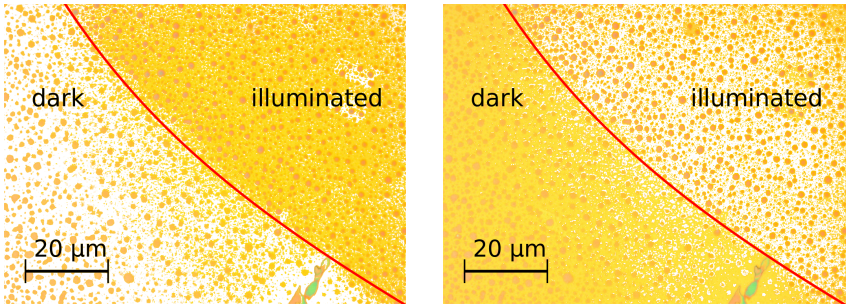

(a) (b)

Figure 42 – The image from Figure 29 manipulated with the color selection tool in gimp. Pixels are colored white when and only when they share similar color. This image manipulation is based on RGB values and not on human perception.

Improvement is a subset of change. Often, the complement of improvement is called decline, but we should rather call it trial and error.

— Unknown

ACKNOWLEDGEMENTS

First and foremost I want to thank my supervisors Prof Günter Reiter and Dr Jean-Luc Bubendorff for their guidance, discussions, insights and also for how they worked together in this french-german cooperation: it felt as if there was no border between the two countries. I also want to thank Dr Laurent Simon for the very fruitful discussions, and both his encouragement and teaching (especially concerning AFM and STM).

I stand in deep gratitude to Dr Sajedeh Motamen, who not only guided me through my master thesis, but continued to work with me, as we shared a common topic in our PhD thesis. In fact I view my thesis as a continuation on the topic, and would like to see another student following our path. In the group from Freiburg I want to thank all my colleagues with whom I shared lab sessions, discussions, presentations and so much more. Namely Dr Asad Jamal, for his calm way in lab, you taught me both the grace and power of being patient. Dr Renate Reiter, Dr Stephan Laule, Dr Benjamin Winkler and (later) Dr Thomas Pfohl, for much more than just sharing an office: you made even hard times fun, and fun times even funnier. Dr Sivasurender Chandran for many helpful discussions and also the fun outside office. Dr Sumit Majumder, Dr Purushottam Poudel and Rishab Handa for teaching me about India, an unforgettable cooking session and uncountable hours in the lab. A big thank you goes to Barbara Heck for her help with WAXS experiments. A very special thanks to Silvia Siegenführ, the heart of the group - not only for her support in lab (and most often out of plain view), but also for always finding the right words even in hard times.

I also want to thank the french group in Mulhouse for their warm welcome. Dr Lakshya Daukiya, for lots of interesting discussions. Alban for teaching me quite some french. Francois and Marion for the shared lunches; I enjoyed french cuisine a lot.

I received another warm welcome in the group of Prof Thomas Heiser in Strasbourg. Thanks to him and Sadiara Fall, for the access to the lab, the introduction to the equipment, lending uncounted helping hands and the passionate discussions about the results.

I want to thank several of my friends who accompanied me during this time. A huge thank you to Ente Pankopf, Nico Offedu, Matthias Dold and Dr Lucas Flatten for the awesome time we had, namely campfire evenings, balloon and bike rides, sauna and hot baths, Doppelkopf, Skat and other card games, introducing me to even more awesome people and so much more. Thanks to Georg Hoppe, for all of the above, and for being like a second brother to me. Anne Theis and Lisa Atmanspacher, it seems some things never change, and I'm glad they don't. Dr Ana Perez, for someone I just met in a conference, up to this day it feels so much closer than just sharing a similar PhD topic. I hope you'll invent either a teleporter or a time travel at some point in the future, but for the time being I'm satisfied with a time bubble machine, too. There's no stepping stone big enough to stop you.

And of course a huge thank you to Ronja Zirm, for sharing all the things I love, and for never stopping to be a friend.

Last but not least I want to thank my family for all their support. My brother, for discussing it out, cheering me up or distracting me, whenever need be. And for magically knowing better than myself which one I need. My parents, for being friends in addition to being parents, for forgiving my mistakes, and especially for providing a safety net to fall back into. And to my grandparents, for setting everything surrounding my life up the way I love it.

This thesis is dedicated to my grandma, who feared that she may not be allowed to call for me without using my correct title once I had finished. For you I had always stayed just Sven, and I wish I could have finished earlier... I will never forget both your pride and respect for that title. And I will not forget that this is a huge privilege.

BIBLIOGRAPHY

[1] Ph. Avouris and In-Whan Lyo. « Probing and inducing surface chemistry with the STM: the reactions of Si(111)-7x7 with H2O and O2. » In: *Surface Science* 242 (1990), pp. 1–11. DOI: 10.1016/0039-6028(91)90233-I.

[2] Vencenzo Balzani, Alberto Credi, and Margherita Venturi. « Light powered molecular machines. » In: *Chemical Society Reviews* 38 (6 Mar. 2009), pp. 1542–1550. DOI: 10.1039/B806328C.

[3] W. Barthlott and C. Neinhuis. « Purity of the sacred lotus, or escape from contamination in biological surfaces. » In: *Planta* 202 (1 Apr. 1997), pp. 1–8. DOI: 10.1007/s004250050096. URL: https://doi.org/10.1007/s004250050096.

[4] Claire Berger et al. « Ultrathin Epitaxial Graphite: 2D Electron Gas Properties and a Route toward Graphene-based Nanoelectronics. » In: *The Journal of Physical Chemistry B* 108.52 (2004), pp. 19912–19916. DOI: 10.1021/jp040650f.

[5] G. Binnig, Ch. Gerber, E. Stoll, T. R. Albrecht, and C. F. Quate. « Atomic Resolution with Atomic Force Microscope. » In: *EPL (Europhysics Letters)* 3.12 (1987), p. 1281. URL: http://stacks.iop.org/0295-5075/3/i=12/a=006.

[6] G. Binnig, C. F. Quate, and Ch. Gerber. « Atomic Force Microscope. » In: *Phys. Rev. Lett.* 56 (9 Mar. 1986), pp. 930–933. DOI: 10.1103/PhysRevLett.56.930. URL: https://link.aps.org/doi/10.1103/PhysRevLett.56.930.

[7] G. Binnig and H. Rohrer. « Scanning tunneling microscopy. » In: *Surface Science* 126.1 (1983), pp. 236–244. ISSN: 0039-6028. DOI: https://doi.org/10.1016/0039-6028(83)90716-1. URL: http://www.sciencedirect.com/science/article/pii/0039602883907161.

[8] G. Binnig, H. Rohrer, Ch. Gerber, and E. Weibel. « Surface Studies by Scanning Tunneling Microscopy. » In: *Phys. Rev. Lett.* 49 (1 June 1982), pp. 57–61. DOI: 10.1103/PhysRevLett.49.57. URL: https://link.aps.org/doi/10.1103/PhysRevLett.49.57.

[9] G. Binnig and D. P. E. Smith. « Single-tube three-dimensional scanner for scanning tunneling microscopy. » In: *Review of Scientific Instruments* 57.8 (1986), pp. 1688–1689. DOI: 10.1063/1.1139196. eprint: https://doi.org/10.1063/1.1139196. URL: https://doi.org/10.1063/1.1139196.

[10] M. Bode. « Spin-polarized scanning tunnelling microscopy. » In: *Reports on Progress in Physics* 66.4 (2003), p. 523. URL: http://stacks.iop.org/0034-4885/66/i=4/a=203.

[11] John J. Boland. « Manipulating Chlorine Atom Bonding on the Si(100)-(2x1) Surface with the STM. » In: *Science* 262.5140 (1993), pp. 1703–1706. DOI: 10.1126/science.262.5140.1703.

[12] T. L. Boteat and B. Lalevic. « Pd-MOS hydrogen and hydrocarbon sensor device. » In: *Electron Device Letters* 2 (4 Apr. 1981), pp. 82–84. DOI: 10.1109/EDL.1981.25349.

[13] Sivasurender Chandran and Günter Reiter. « Transient Cooperative Processes in Dewetting Polymer Melts. » In: *Phys. Rev. Lett.* 116 (8 Feb. 2016), p. 088301. DOI: 10.1103/PhysRevLett.116.088301. URL: https://link.aps.org/doi/10.1103/PhysRevLett.116.088301.

[14] C. Chubb, G. Sperling, and J. A. Solomon. « Texture interactions determine perceived contrast. » In: *Proceedings of the National Academy of Sciences USA* 86.23 (1989), pp. 9631–9635.

[15] D. M. Eigler and E. K. Schweizer. « Positioning single atoms with a scanning tunnelling microscope. » In: *Nature* 344 (1990), pp. 524–526. DOI: 10.1038/344524a0.

[16] J. S. Foster, J. E. Frommer, and P. C. Arnett. « Molecular manipulation using a tunnelling microscope. » In: *Nature* 331 (1988), pp. 324–326. DOI: 10.1038/331324a0.

[17] Werner Frammelsberger, Guenther Benstetter, Janice Kiely, and Richard Stamp. « C-AFM-based thickness determination of thin and ultra-thin SiO2 films by use of different conductive-coated probe tips. » In: *Applied Surface Science* 253.7 (2007), pp. 3615–3626. ISSN: 0169-4332. DOI: https://doi.org/10.1016/j.apsusc.2006.07.070.

[18] Wouter H van Geffen, Marcel Bruins, and Huib A M Kerstjens. « Diagnosing viral and bacterial respiratory infections in acute COPD exacerbations by an electronic nose: a pilot study. » In:

Journal of Breath Research 10.3 (June 2016), p. 036001. DOI: 10.1088/1752-7155/10/3/036001.

[19] F J Giessibl, S Hembacher, M Herz, Ch Schiller, and J Mannhart. « Stability considerations and implementation of cantilevers allowing dynamic force microscopy with optimal resolution: the qPlus sensor. » In: *Nanotechnology* 15.2 (2004), S79. DOI: 10.1088/0957-4484/15/2/017. URL: http://stacks.iop.org/0957-4484/15/i=2/a=017.

[20] Sylvain L. Gilat, Stephen H. Kawai, Jean-Marie Lehn, and Kawai. « Light-Triggered Molecular Devices: Photochemical Switching Of optical and Electrochemical Properties in Molecular Wire Type Diarylethene Species. » In: *Chemistry A European Journal* 1 (5 Aug. 1995), pp. 275–284. DOI: 10.1002/chem.19950010504.

[21] A. J. Heeger and A. G. MacDiarmid. « Polyacetylene, (CH)/sub x/, as an emerging material for solar cell applications. Technical progress report, October, November, December 1979. » In: (Feb. 1980). DOI: 10.2172/5430541.

[22] Saw-Wai Hla, Ludwig Bartels, Gerhard Meyer, and Karl-Heinz Rieder. « Inducing All Steps of a Chemical Reaction with the Scanning Tunneling Microscope Tip: Towards Single Molecule Engineering. » In: *Phys. Rev. Lett.* 85 (13 Sept. 2000), pp. 2777–2780. DOI: 10.1103/PhysRevLett.85.2777. URL: https://link.aps.org/doi/10.1103/PhysRevLett.85.2777.

[23] Mario Hofmann, Wan-Yu Chiang, Tuân D Nguyen, and Ya-Ping Hsieh. « Controlling the properties of graphene produced by electrochemical exfoliation. » In: *Nanotechnology* 26.33 (July 2015), p. 335607. DOI: 10.1088/0957-4484/26/33/335607.

[24] Wael Hourani, Khosrow Rahimi, Ioan Botiz, Felix Peter Vinzenz Koch, Günter Reiter, Peter Lienerth, Thomas Heiser, Jean-Luc Bubendorff, and Laurent Simon. « Anisotropic charge transport in large single crystals of pi-conjugated organic molecules. » In: *Nanoscale* 6 (9 2014), pp. 4774–4780. DOI: 10.1039/C3NR05858A. URL: http://dx.doi.org/10.1039/C3NR05858A.

[25] Fei Hui, Pujashree Vajha, Yuanyuan Shi, Yanfeng Ji, Huiling Duan, Andrea Padovani, Luca Larcher, Xiao Rong Li, Jing Juan Xu, and Mario Lanza. « Moving graphene devices from lab to market: advanced graphene-coated nanoprobes. » In: *Nanoscale* 8 (16 2016), pp. 8466–8473. DOI: 10.1039/C5NR06235G.

[26] H. Kallmann and M. Pope. « Bulk Conductivity in Organic Crystals. » In: *Nature* 186 (1960), pp. 31–33. DOI: 10.1038/186031a0.

[27] H. Kallmann and M. Pope. « Positive Hole Injection into Organic Crystals. » In: *The Journal of Chemical Physics* 32.1 (1960), pp. 300–301. DOI: 10.1063/1.1700925.

[28] M. Lanza, A. Bayerl, T. Gao, M. Porti, M. Nafria, G. Y. Jing, Y. F. Zhang, Z. F. Liu, and H. L. Duan. « Graphene-Coated Atomic Force Microscope Tips for Reliable Nanoscale Electrical Characterization. » In: *Advanced Materials* 25.10 (2013), pp. 1440–1444. DOI: 10.1002/adma.201204380.

[29] Xueming Li, Shu Ping Lau, Libin Tang, Rongbin Ji, and Peizhi Yang. « Sulphur doping: a facile approach to tune the electronic structure and optical properties of graphene quantum dots. » In: *Nanoscale* 6 (10 2014), pp. 5323–5328. DOI: 10.1039/C4NR00693C.

[30] Sandrine Lois, Jean-Charles Florès, Jean-Pierre Lère-Porte, Françoise Serein-Spirau, Joël J. E. Moreau, Karinne Miqueu, Jean-Marc Sotiropoulos, Patrick Baylère, Monique Tillard, and Claude Belin. « How to Build Fully Pi-Conjugated Architectures with Thienylene and Phenylene Fragments. » In: *European Journal of Organic Chemistry* 2007.24 (), pp. 4019–4031. DOI: 10.1002/ejoc.200601114. eprint: https://onlinelibrary.wiley.com/doi/pdf/10.1002/ejoc.200601114. URL: https://onlinelibrary.wiley.com/doi/abs/10.1002/ejoc.200601114.

[31] Wilhelm Melitz, Jian Shen, Andrew C. Kummel, and Sangyeob Lee. « Kelvin probe force microscopy and its application. » In: *Surface Science Reports* 66.1 (2011), pp. 1–27. ISSN: 0167-5729. DOI: https://doi.org/10.1016/j.surfrep.2010.10.001. URL: http://www.sciencedirect.com/science/article/pii/S0167572910000841.

[32] Sajedeh Motamen, Dominic Raithel, Richard Hildner, Khosrow Rahimi, Thibaut Jarrosson, Françoise Serein-Spirau, Laurent Simon, and Günter Reiter. « Revealing Order and Disorder in Films and Single Crystals of a Thiophene-Based Oligomer by Optical Spectroscopy. » In: *ACS Photonics* 3.12 (2016), pp. 2315–2323. DOI: 10.1021/acsphotonics.6b00473. URL: https://doi.org/10.1021/acsphotonics.6b00473.

[33] Sajedeh Motamen, Christian Schorner, Dominic Raithel, Jean-Pierre Malval, Thibaut Jarrosson, Francoise Serein-Spirau, Laurent Simon, Richard Hildner, and Gunter Reiter. « Low loss op-

tical waveguiding in large single crystals of a thiophene-based oligomer. » In: *Phys. Chem. Chem. Phys.* 19 (24 2017), pp. 15980–15987. DOI: 10.1039/C7CP01639E. URL: http://dx.doi.org/10.1039/C7CP01639E.

[34] M. P. Murrell, M. E. Welland, S. J. O'Shea, T. M. H. Wong, J. R. Barnes, A. W. McKinnon, M. Heyns, and S. Verhaverbeke. « Spatially resolved electrical measurements of SiO2 gate oxides using atomic force microscopy. » In: *Applied Physics Letters* 62.7 (1993), pp. 786–788. DOI: 10.1063/1.108579.

[35] Maya Narayanan Nair et al. « One- and two-photon absorption and emission properties of an oligo(phenylenethienylene)s series. » In: *Phys. Chem. Chem. Phys.* 16 (25 2014), pp. 12826–12837. DOI: 10.1039/C2CP44365A. URL: http://dx.doi.org/10.1039/C2CP44365A.

[36] M. Nonnenmacher, M. P. O'Boyle, and H. K. Wickramasinghe. « Kelvin probe force microscopy. » In: *Applied Physics Letters* 58.25 (1991), pp. 2921–2923. DOI: 10.1063/1.105227.

[37] Y. Okawa and M. Aono. « Linear chain polymerization initiated by a scanning tunneling microscope tip at designated positions. » In: *The Journal of Chemical Physics* 115.5 (2001), pp. 2317–2322. DOI: 10.1063/1.1384554. eprint: https://doi.org/10.1063/1.1384554. URL: https://doi.org/10.1063/1.1384554.

[38] Y. Okawa and M. Aono. « Nanoscale control of chain polymerization. » In: *Nature* 409 (2001), pp. 683–684. DOI: 10.1038/35055625.

[39] Jian Pei, Wang-Lin Yu, Wei Huang, and Alan J. Heeger. « A Novel Series of Efficient Thiophene-Based Light-Emitting Conjugated Polymers and Application in Polymer Light-Emitting Diodes. » In: *Macromolecules* 33.7 (2000), pp. 2462–2471. DOI: 10.1021/ma9914220.

[40] Guido Raos, Antonino Famulari, Stefano V. Meille, Maria C. Gallazzi, and Giuseppe Allegra. « Interplay of Conformational States and Nonbonded Interactions in Substituted Bithiophenes. » In: *The Journal of Physical Chemistry A* 108.4 (2004), pp. 691–698. DOI: 10.1021/jp036614i. eprint: https://doi.org/10.1021/jp036614i. URL: https://doi.org/10.1021/jp036614i.

[41] Günter Reiter. « Dewetting of Highly Elastic Thin Polymer Films. » In: *Phys. Rev. Lett.* 87 (18 Oct. 2001), p. 186101. DOI: 10.1103/PhysRevLett.87.186101. URL: https://link.aps.org/doi/10.1103/PhysRevLett.87.186101.

[42] Daniel Rugar and Paul Hansma. « Atomic Force Microscopy. » In: *Physics Today* 43.10 (1990), pp. 23–30. DOI: 10.1063/1.881238.

[43] R. Seemann, S. Herminghaus, and K. Jacobs. « Dewetting Patterns and Molecular Forces: A Reconciliation. » In: *Phys. Rev. Lett.* 86 (24 June 2001), pp. 5534–5537. DOI: 10.1103/PhysRevLett.86.5534. URL: https://link.aps.org/doi/10.1103/PhysRevLett.86.5534.

[44] Hideki Shirakawa, Edwin J. Louis, Alan G. MacDiarmid, Chwan K. Chiang, and Alan J. Heeger. « Synthesis of electrically conducting organic polymers: halogen derivatives of polyacetylene, (CH). » In: *J. Chem. Soc., Chem. Commun.* (16 1977), pp. 578–580. DOI: 10.1039/C39770000578.

[45] Roozbeh Shokri et al. « Generating Long Supramolecular Pathways with a Continuous Density of States by Physically Linking Conjugated Molecules via Their End Groups. » In: *Journal of the American Chemical Society* 135.15 (2013). PMID: 23517379, pp. 5693–5698. DOI: 10.1021/ja311964b. eprint: https://doi.org/10.1021/ja311964b. URL: https://doi.org/10.1021/ja311964b.

[46] Chris Timms, Paul S Thomas, and Deborah H Yates. « Detection of gastro-oesophageal reflux disease (GORD) in patients with obstructive lung disease using exhaled breath profiling. » In: *Journal of Breath Research* 6.1 (Jan. 2012), p. 016003. DOI: 10.1088/1752-7155/6/1/016003.

[47] F. Vonau et al. « Branched Substituents Generate Improved Supramolecular Ordering in Physisorbed Molecular Assemblies. » In: *The Journal of Physical Chemistry C* 113.12 (2009), pp. 4955–4959. DOI: 10.1021/jp809552j.

[48] R. Wiesendanger, H.-J. Güntherodt, G. Güntherodt, R. J. Gambino, and R. Ruf. « Observation of vacuum tunneling of spin-polarized electrons with the scanning tunneling microscope. » In: *Phys. Rev. Lett.* 65 (2 July 1990), pp. 247–250. DOI: 10.1103/PhysRevLett.65.247. URL: https://link.aps.org/doi/10.1103/PhysRevLett.65.247.

[49] Dedy Rahman Wijaya, Riyanarto Sarno, Enny Zulaika, and Shoffi Izza Sabila. « Development of mobile electronic nose for beef quality monitoring. » In: *Procedia Computer Science* 124 (2017). 4th Information Systems International Conference 2017, ISICO 2017, 6-8 November 2017, Bali, Indonesia, pp. 728–735. ISSN: 1877-0509. DOI: https://doi.org/10.1016/j.procs.2017.12.211. URL: http://www.sciencedirect.com/science/article/pii/S1877050917329794.

[50] Alphus D. Wilson and Manuela Baietto. « Applications and Advances in Electronic-Nose Technologies. » In: *Sensors* 9 (May 2009), pp. 5099–5148. DOI: 10.3390/s90805099.

[51] R. Xie, A. Karim, J. F. Douglas, C. C. Han, and R. A. Weiss. « Spinodal Dewetting of Thin Polymer Films. » In: *Phys. Rev. Lett.* 81 (6 Aug. 1998), pp. 1251–1254. DOI: 10.1103/PhysRevLett.81.1251. URL: https://link.aps.org/doi/10.1103/PhysRevLett.81.1251.

DECLARATION

Ich erkläre hiermit, dass ich die vorliegende Arbeit ohne unzulässige Hilfe Dritter und ohne Benutzung anderer als der angegebenen Hilfsmittel angefertigt habe. Die aus anderen Quellen direkt oder indirekt übernommenen Daten und Konzepte sind unter Angabe der Quelle gekennzeichnet. Insbesondere habe ich hierfür nicht die entgeltliche Hilfe von Vermittlungs- beziehungsweise Beratungsdiesten (Promotionsberater/-beraterinnen oder anderer Personen) in Anspruch genommen.

Freiburg, January 2021

Sven Renkert

COLOPHON

This document was typeset using the typographical look-and-feel `classicthesis` developed by André Miede. The style was inspired by Robert Bringhurst's seminal book on typography "*The Elements of Typographic Style*". `classicthesis` is available for both LaTeX and LyX:

https://bitbucket.org/amiede/classicthesis/

Happy users of `classicthesis` usually send a real postcard to the author, a collection of postcards received so far is featured here:

http://postcards.miede.de/

Final Version as of 9. Januar 2021 (`classicthesis` Version 1.0).